

CrossMark  
click for updates

## Opinion piece

**Cite this article:** Uhlirova H *et al.* 2016The roadmap for estimation of cell-type-specific neuronal activity from non-invasive measurements. *Phil. Trans. R. Soc. B* **371**: 20150356.<http://dx.doi.org/10.1098/rstb.2015.0356>

Accepted: 14 July 2016

One contribution of 15 to a Theo Murphy meeting issue 'Interpreting BOLD: a dialogue between cognitive and cellular neuroscience'.

**Subject Areas:**

neuroscience

**Keywords:**BOLD fMRI, CMRO<sub>2</sub>, magnetoencephalography, neurovascular, neurometabolic, cerebral blood flow**Author for correspondence:**

Anna Devor

e-mail: [adevor@ucsd.edu](mailto:adevor@ucsd.edu)

## The roadmap for estimation of cell-type-specific neuronal activity from non-invasive measurements

Hana Uhlirova<sup>1,17</sup>, Kivilcim Kılıç<sup>2</sup>, Peifang Tian<sup>2,9</sup>, Sava Sakadžić<sup>10</sup>, Louis Gagnon<sup>10</sup>, Martin Thunemann<sup>1</sup>, Michèle Desjardins<sup>1</sup>, Payam A. Saisan<sup>2</sup>, Krystal Nizar<sup>3</sup>, Mohammad A. Yaseen<sup>10</sup>, Donald J. Hagler Jr<sup>1</sup>, Matthieu Vandenberghe<sup>1,11</sup>, Srdjan Djurovic<sup>12,13</sup>, Ole A. Andreassen<sup>11</sup>, Gabriel A. Silva<sup>4,5</sup>, Eliezer Masliah<sup>2</sup>, David Kleinfeld<sup>6,7,8</sup>, Sergei Vinogradov<sup>14</sup>, Richard B. Buxton<sup>1</sup>, Gaute T. Einevoll<sup>15,16</sup>, David A. Boas<sup>10</sup>, Anders M. Dale<sup>1,2</sup> and Anna Devor<sup>1,2,10</sup><sup>1</sup>Department of Radiology, <sup>2</sup>Department of Neurosciences, <sup>3</sup>Neurosciences Graduate Program, <sup>4</sup>Department of Bioengineering, <sup>5</sup>Department of Ophthalmology, <sup>6</sup>Department of Physics, <sup>7</sup>Department of Electrical and Computer Engineering, and <sup>8</sup>Section of Neurobiology, UCSD, La Jolla, CA 92093, USA<sup>9</sup>Department of Physics, John Carroll University, University Heights, OH 44118, USA<sup>10</sup>Martinos Center for Biomedical Imaging, MGH, Harvard Medical School, Charlestown, MA 02129, USA<sup>11</sup>NORMENT, KG Jebsen Centre for Psychosis Research, Division of Mental Health and Addiction, Oslo University Hospital and University of Oslo, 0407 Oslo, Norway<sup>12</sup>Department of Medical Genetics, Oslo University Hospital, 0407 Oslo, Norway<sup>13</sup>NORMENT, KG Jebsen Centre for Psychosis Research, Department of Clinical Science, University of Bergen, 5020 Bergen, Norway<sup>14</sup>Department of Biochemistry and Biophysics, University of Pennsylvania, Philadelphia, PA 19104, USA<sup>15</sup>Department of Mathematical Sciences and Technology, Norwegian University of Life Sciences, 1432 Ås, Norway<sup>16</sup>Department of Physics, University of Oslo, 0316 Oslo, Norway<sup>17</sup>CEITEC – Central European Institute of Technology and Institute of Physical Engineering, Faculty of Mechanical Engineering, Brno University of Technology, Brno, Czech Republic

ID LG, 0000-0001-7202-5176; DK, 0000-0001-9797-4722

The computational properties of the human brain arise from an intricate interplay between billions of neurons connected in complex networks. However, our ability to study these networks in healthy human brain is limited by the necessity to use non-invasive technologies. This is in contrast to animal models where a rich, detailed view of cellular-level brain function with cell-type-specific molecular identity has become available due to recent advances in microscopic optical imaging and genetics. Thus, a central challenge facing neuroscience today is leveraging these mechanistic insights from animal studies to accurately draw physiological inferences from non-invasive signals in humans. On the essential path towards this goal is the development of a detailed 'bottom-up' forward model bridging neuronal activity at the level of cell-type-specific populations to non-invasive imaging signals. The general idea is that specific neuronal cell types have identifiable signatures in the way they drive changes in cerebral blood flow, cerebral metabolic rate of O<sub>2</sub> (measurable with quantitative functional Magnetic Resonance Imaging), and electrical currents/potentials (measurable with magneto/electroencephalography). This forward model would then provide the 'ground truth' for the development of new tools for tackling the inverse problem—estimation of neuronal activity from multimodal non-invasive imaging data.

This article is part of the themed issue 'Interpreting BOLD: a dialogue between cognitive and cellular neuroscience'.

## 1. Introduction

Today, most major programmes in Neuroscience and Psychology have their own functional imaging systems and laboratories. We can assess haemodynamic

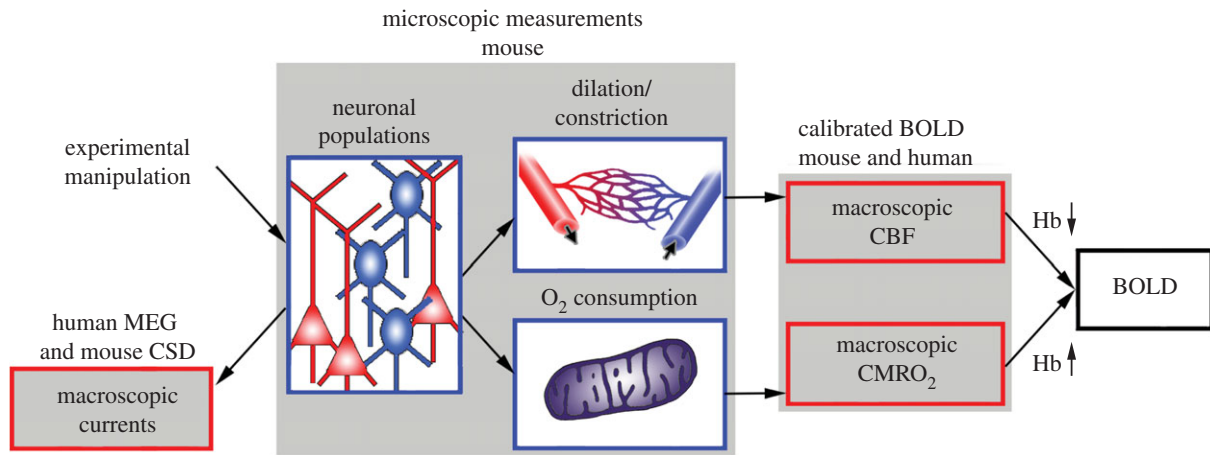


**Figure 1.** Conceptual relationship between physiological parameters and measurements in mice and humans across scales. Advancing our ability to infer microscopic details of underlying physiology in the human brain from non-invasive methods requires parallel data acquisition in animals (e.g. mice) and humans, and a complementary theoretical effort building computational bridges between the varying scales as well as from animals to humans. Animal experiments are necessary to directly measure and manipulate concrete cellular-level physiological parameters. These measurements, which are only available in model organisms, provide the microscopic ‘ground truth’ needed for the development of theoretical models. In parallel, multimodal non-invasive human data are needed to evaluate translation.

changes with functional Magnetic Resonance Imaging (fMRI) and functional Near-Infrared Spectroscopy, broad regional electrical activity with magneto/electroencephalography (MEG/EEG) and metabolism/neurochemistry with Positron Emission Tomography. And yet, despite this widespread adoption, the power of available human neuroimaging methods remains limited, leaving a gap between the macroscopic activity patterns available in humans and the rich, detailed view achievable in model organisms. Thus, a central challenge facing neuroscience today is leveraging these mechanistic insights from animal studies to accurately draw physiological inferences from non-invasive signals in humans, essentially asking the fundamental question: what information about neuronal circuit activity can we reliably determine from non-invasive functional imaging in humans? This question has been approached by many investigators in different ways [1–6], and our goal is not to provide a detailed review of this work. Instead, in this opinion article our goal is to outline a particular approach—a roadmap—based on our recent work that has the potential to provide the basis for a deeper interpretation of functional imaging in humans.

Our specific focus is on the physiological underpinning of Blood Oxygenation Level Dependent (BOLD) fMRI [7,8] combined with MEG/EEG [9,10] in the healthy cerebral cortex. The central physiological phenomenon underlying the BOLD effect is that, in areas that experience an increase in neuronal activity, cerebral blood flow (CBF) usually increases much more than cerebral metabolic rate of oxygen (CMRO<sub>2</sub>), leading to an increase in blood and tissue oxygenation that drives the BOLD fMRI signal up. The biological function of this imbalance of CBF and CMRO<sub>2</sub> is still not fully understood, but is likely to be a mechanism to prevent the tissue O<sub>2</sub> concentration from falling when CMRO<sub>2</sub> increases [2,11–13]. Thus, the BOLD signal reflects neuronal activity only indirectly through its relationship with CBF and CMRO<sub>2</sub>. Furthermore, increasing CBF and CMRO<sub>2</sub> pushes the BOLD signal in opposite directions adding to the difficulty in interpretation (figure 1). If the ratio of CBF and CMRO<sub>2</sub> changes remained constant, the BOLD signal could still be a reliable metric for the magnitude of neuronal activity change, but there is now substantial evidence that CBF/CMRO<sub>2</sub> coupling varies in the same brain region with stimulus intensity, attention, adaptation and after ingestion of caffeine [14,15].

As a result of these limitations, in current practice we do not know how to interpret BOLD fMRI studies in terms of the underlying brain physiology even at the vascular/haemodynamic level in the healthy human brain, let alone in ageing and disease. The intrinsic ambiguities of the BOLD signal underscore the importance of a multimodal imaging approach [16]. The motivation for the current paper is the idea that, while the BOLD signal alone is fundamentally ambiguous, the combination of BOLD imaging with arterial spin labelling (ASL) methods and the ‘calibrated BOLD’ approach (a.k.a. ‘quantitative fMRI’) makes it possible to isolate the effects of CBF and CMRO<sub>2</sub>—the macroscopic physiological parameters directly related to neurovascular and neurometabolic coupling [17–19]. This means that neuronal activity patterns that differentially affect CBF and CMRO<sub>2</sub> (e.g. net excitation versus net inhibition) may be distinguishable with calibrated BOLD. Furthermore, more detailed, time-resolved information about activity of cell-type-specific neuronal populations may become available from a combination of calibrated BOLD with MEG/EEG, as long as these populations differentially contribute to macroscopic electrical signals detectable from the brain surface.

We emphasize cell-type-specific populations rather than single neurons because brains of mammals, including mice and humans, appear to be built from large populations of neurons collectively performing similar function in a probabilistic way. This is in contrast to invertebrates such as the nematode *Caenorhabditis elegans* where a few individually identified neurons can govern specific behaviours [20]. Thus, for human neuroimaging, interpreting the data in terms of the respective activity levels of cell-type-specific neuronal populations may be sufficient for understanding circuit dynamics.

The ongoing large initiatives such as The BRAIN Initiative in the US and the Human Brain Project in Europe, which aim to develop new experimental and computational technologies and platforms, will undoubtedly advance our ability to probe functional organization of the human brain [21–23]. However, already today we can start tackling the challenge of extracting cell-type-specific neuronal activity from non-invasive imaging by designing parallel experiments in animals and humans, integrating existing measurement modalities and building computational bridges across scales.

To illustrate this approach, we focus on the primary somatosensory cortex (SI) where ‘bottom-up’ models can be built and calibrated taking advantage of well-studied neuronal network phenomena such as the surround and transcallosal inhibition [24–29]. In animals (e.g. mice), we can use microscopic measurement technologies to precisely and quantitatively probe concrete microscopic neuronal, vascular and metabolic parameters while manipulating cell-type-specific neuronal activity (figure 1, blue boxes). These microscopic data can then be used to simulate the corresponding macroscopic physiological parameters (CBF, CMRO<sub>2</sub> and current dipole moment) and their reflection in non-invasive observables (figure 1, red boxes) [30–32]. Thus, in mice, we can develop a detailed forward model bridging neuronal activity at the level of cell-type-specific populations to non-invasive imaging signals. Furthermore, we can validate this model at each step against real data. For human translation, first we would have to calibrate the model parameters to account for systematic differences due to known physical scaling laws such as differences in vessel size or latency of the cortical neuronal response. Then, the remaining uncertainty in the translation of model parameters from mouse to human (as well as the measurement noise and subject-to-subject variability) would be factored into a single Bayesian estimation framework [33] to obtain estimates of the parameters of interest (i.e. activity of cell-type-specific neuronal populations) and quantify the uncertainty of estimation.

In this context, the key question is: What is the evidence for the differential vasoactive role, energetic costs and electrical currents/potentials associated with activity of different neuronal cell types? That is, are there cell-type-specific signatures in terms of how activity of a particular type of neurons affects CBF, CMRO<sub>2</sub> and current dipole? If so, multimodal non-invasive imaging could potentially provide a much more specific window on neuronal circuit activity in humans. The remainder of the paper is a roadmap for reaching that end.

## 2. Microscopic regulation of dilation and constriction

A growing body of data increasingly suggests that differential vascular control originates from activation of specific neuronal sub-populations through release of vasoactive signalling molecules [34–45]. *In vitro* (brain slice) studies in cerebral and cerebellar cortices have demonstrated that spiking of specific types of neurons can cause dilation or constriction of nearby arterioles [41,45]. *In vivo* studies revealed a correlation between arteriolar constriction and neuronal inhibition (figure 2*a–e*) [38,46,47]. The vasoconstriction was abolished by blocking of neuronal activity [38] and was found on the arterial side while venous diameters stayed unchanged [48,49] suggesting an active process rather than a passive ‘blood steal’. This conclusion was further supported by a modelling study [30]. These observations are consistent with reports of negative BOLD signals in cortical regions that are expected to experience inhibition such as those surrounding the centre of the neuronal response (a.k.a. ‘surround inhibition’) and in the ipsilateral hemisphere [29,46,50–54]. Some of these studies used simultaneous extracellular recording of multiunit spiking activity to provide evidence of a decrease in neuronal firing (i.e. inhibition) spatially coincident with the negative BOLD signal [46].

Dilation (and constriction) propagates along vascular walls [55–58]. Therefore, identifying the location of the earliest dilation is important for isolation of the local rather than conducted neurovascular mechanisms. A body of work has documented the temporal properties of stimulus-induced diameter changes in surface (pial) arterioles, diving arteriolar trunks, and their initial lateral branches (the first three to four branching orders off the diving trunk) [38,47,59–62]. Two-photon measurements at different depths revealed that the earliest dilation onset occurs in deep cortical layers, below layer IV (in the mouse, dilation in layer V starts approx. 500 ms prior to that in layer I) [63]. The dilation latency gradually increases with decreasing cortical depth (figure 2*f,g*) [59–61,63] and, in the upper layers, also with increasing branching order such that diving trunks precede their side branches (figure 2*h*) [59]. The overall picture is consistent with propagation of dilation from the deep layers towards the cortical surface along diving arterioles, invading lateral arteriolar branches on the way. These findings do not imply that propagation within the vascular wall is the only mechanism behind the observed timing gradients and do not rule out local neurovascular communication in the upper layers. In the presence of both local and conducted signalling, the onset of dilation would be determined by the faster of the two processes. However, substantial delays in the superficial arteriolar branches suggest that local neurovascular communication in the upper layers, if it exists, has slower kinetics. Gaining insight into the mechanisms generating these temporal differences would lead to better understanding of neurovascular coupling.

These temporal gradients are robust in our hands, but remain controversial in the field. As such, the gradual decrease in the latency of dilation with depth is in agreement with a depth-resolved fMRI study in humans [64] but at odds with a recent high-resolution fMRI study in rats [65]. This discrepancy, however, may reflect the complex nature of the BOLD signal that depends on the balance between O<sub>2</sub> delivery and consumption as well as on the measurement theory specific to the chosen data-acquisition paradigm. Two-photon diameter measurements, on the other hand, are direct and assumption-free. A controversy exists also regarding the dependence on the branching order. Specifically, one study reported that stimulus-induced dilation of low-order branches, traditionally known as the ‘precapillary arterioles’, can precede their parent diving arteriolar trunks [62]; the same study unconventionally labelled these low-order branches as capillaries. The reason for the discrepancy between this result and data from our studies is unclear. While the low-order branches (that may include true capillaries) can dilate and constrict, high-order branches, i.e. capillaries in the bulk capillary bed, do not possess contractile elements and therefore lack active dilation or constriction [66–68]. The same applies to veins although a slow and passive increase in the venous volume in response to a steady-state increase in neuronal activity has been reported [69].

Two-photon single-vessel measurements can be combined with optogenetic (OG) stimulation, opening the door to study neurovascular regulation with an unprecedented level of specificity (figure 3*a,b*). Because different types of neurons are wired together in intact cerebral circuits, they are co-activated during neuronal events, e.g. during the responses to an external stimulus. For this reason, isolation of cell-type-specific neuronal activity *in vivo* was virtually impossible prior to the arrival of optogenetics [70]. The currently available OG tools offer both

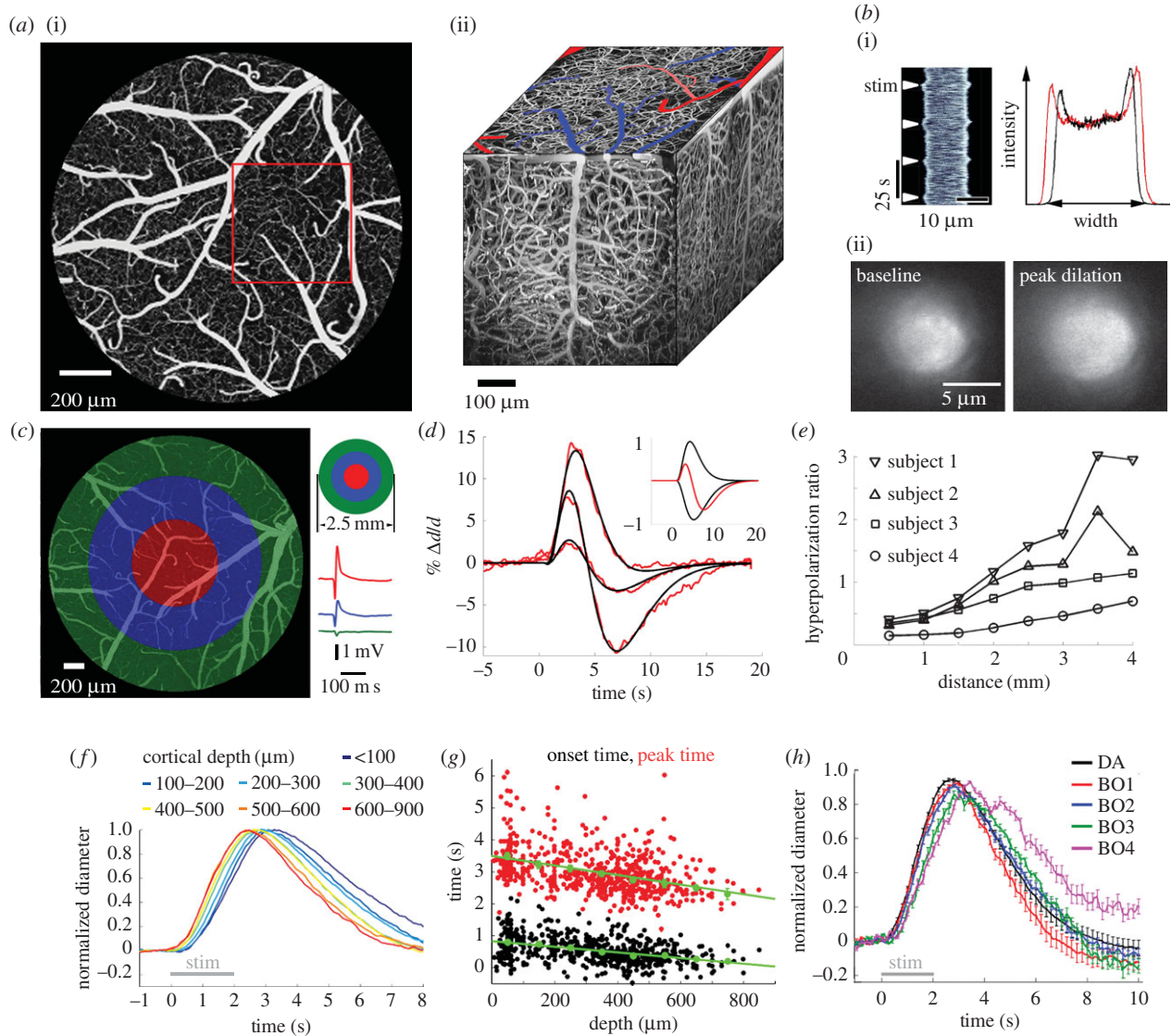


**Figure 2.** Two-photon measurements of dilation and constriction. (a)(i) Top-down maximal intensity projection (MIP) of a low-magnification image stack showing surface vasculature. (ii) Three-dimensional projection from the area outlined in red on the MIP. (b) Line-scan (i) and frame-scan (ii) diameter measurements. (c) Mapping the centre of neuronal response to the stimulus using surface potential recordings. (d) The 'centre-surround' structure of the arteriolar dilation response. Three examples of stimulus-induced arteriolar diameter change (red) at different distances from the centre of evoked neuronal response with overlaid computational fit to the data (black). The inset shows the functions C (positive) and D (negative) used to fit the data. The sum of the two normalized by the maximum of the sum of their absolute values is shown in red in the inset. (e) The surround region with stronger vasoconstriction experiences stronger inhibition. The plot shows the hyperpolarization ratio (the ratio of peak hyperpolarization to peak depolarization) as a function of distance from the centre obtained using voltage-sensitive dye imaging. Data from four animals are superimposed. (f) Sensory stimulus-induced dilation time courses sorted by depth and peak-normalized. Colour-coded depth categories are indicated on top. (g) Onset (black) and time-to-peak (red) of dilation as a function of depth. Each data point represents a single measurement. For each subject, the data were group-averaged according to depth in 100- $\mu\text{m}$  bins. Error bars represent the mean  $\pm$  s.e. across subjects for each bin (green). (h) Sensory stimulus-induced dilation time courses sorted by the branching order (colour-coded). The data were averaged from cortical depth corresponding to layers II–V (100–700  $\mu\text{m}$ ). DA, diving arteriole; BO, branching order.

activation and inactivation of many neuronal cell types [71]. To ensure specificity in such an experiment, care should be taken to prevent the spread of activation to other neuronal cell types. For example, unless synaptic communication is inhibited, OG activation of excitatory pyramidal cells (PCs) may not provide an advantage for the study of neurovascular coupling over sensory stimulation: in both cases firing of many neuronal cell types results in the release of a mixture of neurotransmitters and peptides. Using OG stimulation and two-photon imaging, we recently demonstrated that excitatory and inhibitory neurons drive parallel dilatory pathways while virtually the entire constriction response was explained by Neuropeptide Y (NPY) presumably released from a specific class of inhibitory neurons expressing NPY (figure 3c–h) [63]. OG stimulation can be employed in haemodynamic studies also through

combination with fMRI and single-photon haemodynamic measurements [72–76].

Release of neurotransmitters, neuropeptides and  $\text{K}^+$  from spiking neurons can activate cortical glial cells called astrocytes that have their own repertoire of vasoactive molecular messengers synthesized and released in  $\text{Ca}^{++}$ -dependent way [37,77–82]. Therefore, astrocytes have been hypothesized to mediate neurovascular coupling. However, recent *in vivo* imaging studies from us and others produced experimental evidence inconsistent with this idea showing that, under minimally invasive measurement conditions, the astrocytic  $\text{Ca}^{++}$  excitability (i.e. the presence of either spontaneous or evoked astrocytic  $\text{Ca}^{++}$  surges) is generally low and occurs on the timescale that is too slow to drive dilation (figure 4) [60,83,84]. One recent study arrived at a different conclusion

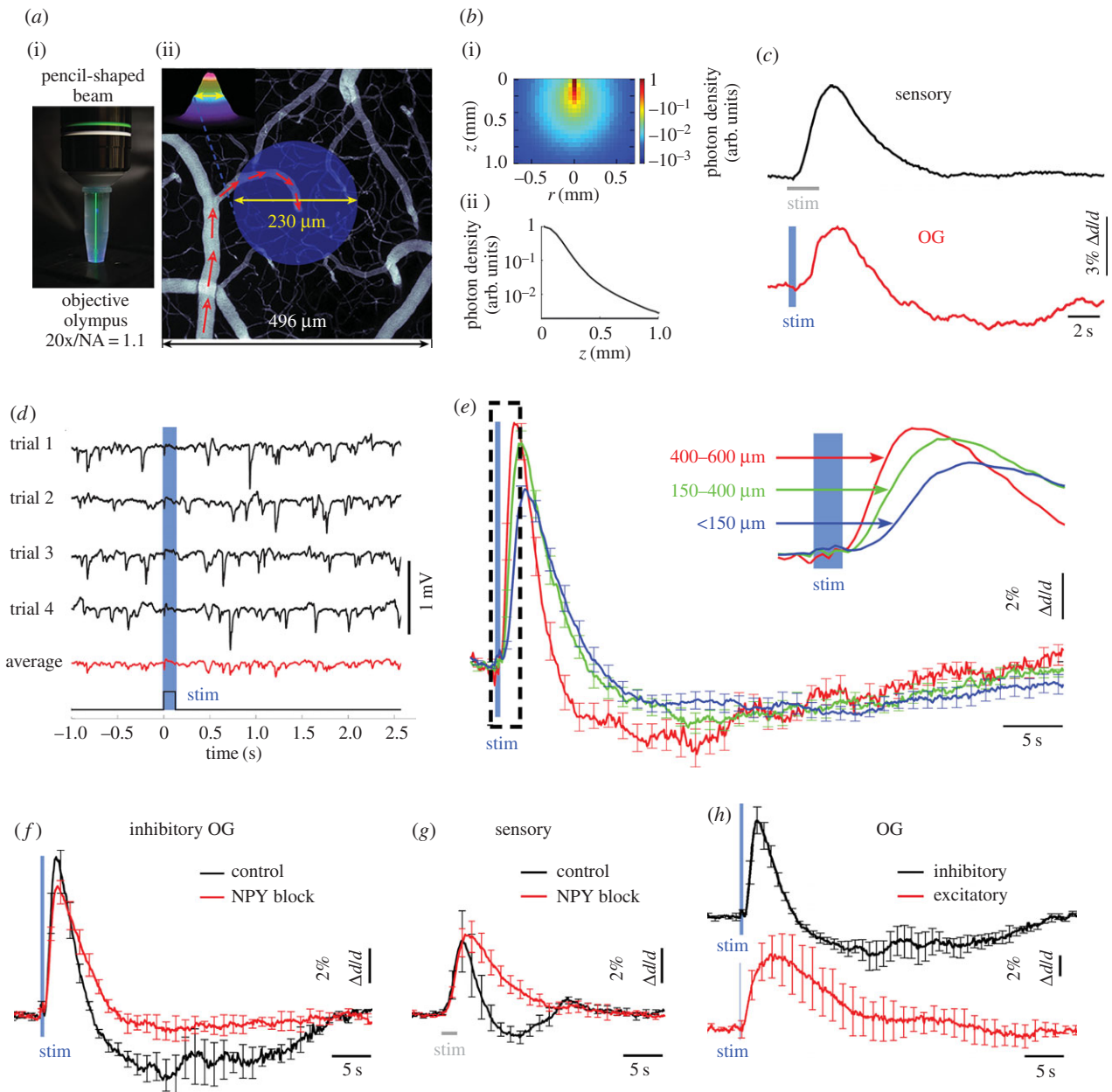


**Figure 3.** Cell-type specificity of neurovascular coupling. (a)(i) The 473 nm laser beam visualized in fluorescent medium, used for OG modulation. (ii) Schematic of the OG beam centred on a diving arteriole. The full width at half maximum (FWHM = 230  $\mu\text{m}$ ) of the beam is superimposed on a vascular mean intensity projection image. Red arrows indicate the direction of flow in the arteriole. (b) Simulated spatial profile of the OG beam in cortical tissue. (i) Colour-coded photon density. (ii) Photon density as a function of depth ( $z$ -axis). (c) Diameter change time courses of the diving arteriole in (a) in response to a sensory (forepaw) stimulus and selective OG stimulation of inhibitory cortical neurons. Ten sensory stimulus trials were averaged. (d) LFP recorded from layer II/III during the OG stimulation of inhibitory cortical neurons. Each trace shows a single stimulus trial. Downward deflections in the LFP signal indicate spontaneous bursts of PCs activity. This behaviour is suppressed during the OG stimulus. (e) Averaged dilation time courses grouped by depth. The inset shows an expanded view of the initial 4 s after the stimulus onset. The depth in micrometres is indicated on the left. Error bars indicate s.e. across subjects. (f) Comparison of dilation time courses in response to OG stimulation of cortical inhibitory neurons before (black) and after (red) blocking Y1 receptors for NPY. Error bars represent s.e. across subjects. (g) As in (f) for the sensory response in the surround area. (h) Comparison of the response to OG stimulation of the inhibitory neurons (also shown in f) to OG stimulation of PCs. Blocker of glutamatergic synaptic transduction were present in the PC experiment to ensure specificity.

showing fast astrocytic kinetics [85]. This fast signal, however, could have resulted from a cross-talk with neuronal  $\text{Ca}^{++}$  activity. Thus, the role of  $\text{Ca}^{++}$ -dependent release of astrocytic vasoactive compounds in CBF regulation remains controversial. In addition, we cannot rule out (currently unknown)  $\text{Ca}^{++}$ -independent pathways as well as a potential astrocytic role in sustaining dilation in response to a long-duration increase in neuronal activity. Furthermore, the phenomenon of glial  $\text{Ca}^{++}$  excitability differs between brain regions [86,87], such that the role of glia in neurovascular communication may not directly translate from one region to the other.

Release of vasoactive messengers is not the only possible neurovascular communication mechanism. In fact, attempts at blocking the dilation response using a cocktail of pharmacological blockers for all known neuronal and astrocytic vasoactive messengers have not been successful [88]. In addition to trivial explanations such as incomplete drug coverage or unknown messenger molecules, the residual dilation may be due to vasoactive metabolites or  $\text{K}^+$ . Vasoactive properties of certain energy metabolites (e.g. lactate and  $\text{CO}_2$ ) are well documented [89–92]. However, cases of dissociation between the dilation response and energy consumption on the microscopic scale *in vivo* suggest

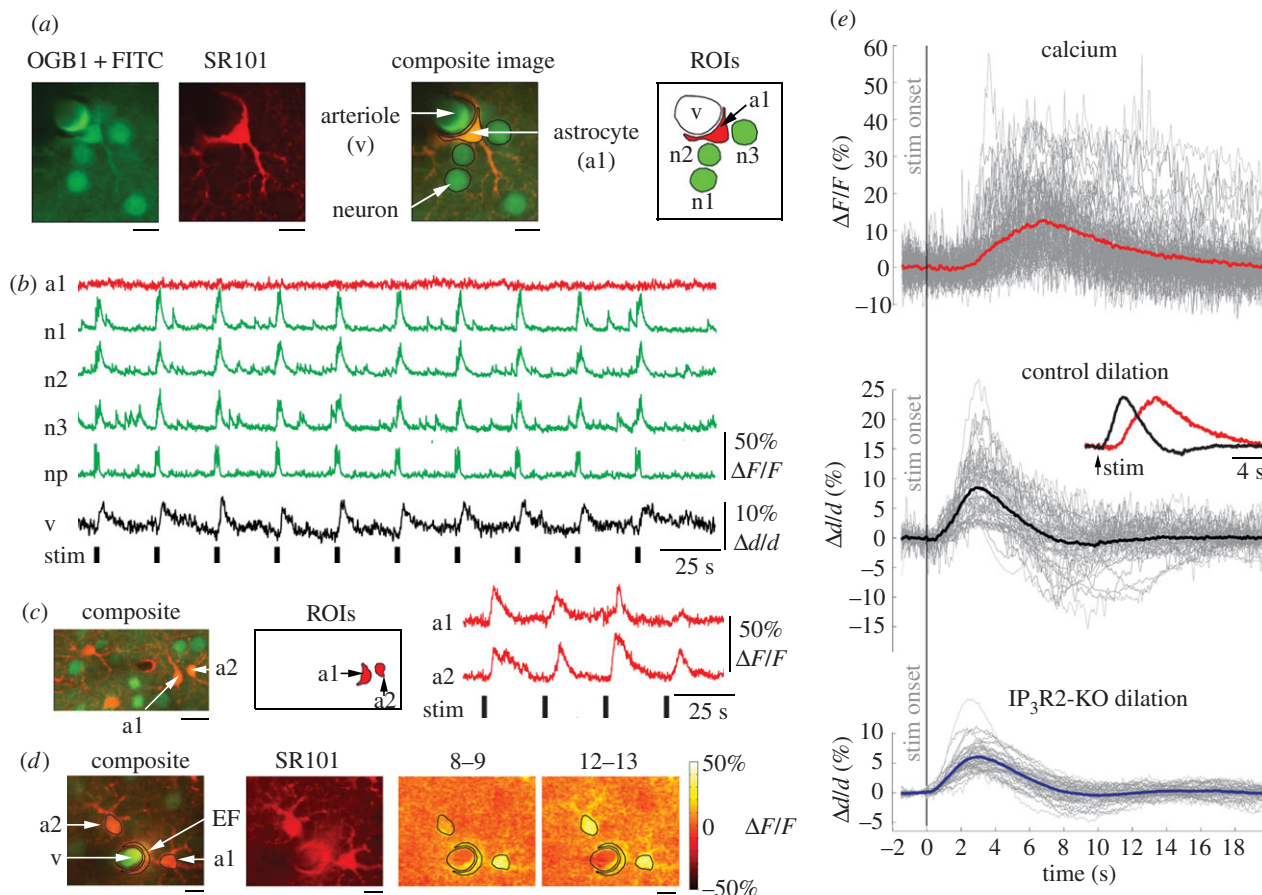


**Figure 4.** Astrocytic  $\text{Ca}^{++}$  response and vasodilation. (a) Representative field of view (FOV) including a perivascular astrocyte labelled with sulforhodamine 101 (SR101) and  $\text{Ca}^{++}$  indicator Oregon Green 488 BAPTA-1 AM (OGB1), a diving arteriole labelled by intravascular injection of fluorescein isothiocyanate (FITC)-labelled dextran, and a number of neuronal cell bodies labelled with OGB1, imaged  $150\ \mu\text{m}$  below the cortical surface. ROIs used for extraction of time courses are shown on the right. Scale bars are  $10\ \mu\text{m}$ . (b) Time courses extracted from the ROIs shown in (a). Astrocytic (red) and neuronal (green)  $\text{Ca}^{++}$  signal changes are expressed as  $\Delta F/F$ . Vasodilation is expressed as per cent diameter change relative to the baseline diameter,  $\Delta d/d$ . The diameter change was extracted from the expansion of FITC-labelled intravascular lumen, indicated by 'v' in (a). The black bars indicate stimulus duration. (c) 'The best' example of astrocytic  $\text{Ca}^{++}$  response to multiple consecutive stimulus trials. Left: FOV imaged  $190\ \mu\text{m}$  below the cortical surface. Middle: ROIs used to extract time courses. Astrocytic  $\text{Ca}^{++}$  signal time courses. Black bars indicate stimulus duration. Scale bars are  $20\ \mu\text{m}$ . (d) An example FOV including two astrocytes, one (a1) with a connected endfoot (EF), imaged  $260\ \mu\text{m}$  below the cortical surface. The EF and a1 contours are overlaid. Each image was computed as an average of 10 consecutive ratio frames. The corresponding time windows (in seconds relative to the stimulus onset) are indicated above the images. Scale bar,  $10\ \mu\text{m}$ . (e) Time-courses of astrocytic  $\text{Ca}^{++}$  change (top) and arteriolar diameter change in control (middle) and in inositol 1,4,5-triphosphate  $\text{IP}_3$  type-2 receptor knock-out ( $\text{IP}_3\text{R2-KO}$ ) mice, in which the primary mechanism of astrocytic  $\text{Ca}^{++}$  increase—the release of  $\text{Ca}^{++}$  from intracellular stores following activation of an  $\text{IP}_3$ -dependent pathway—is lacking (bottom). An average is superimposed on each panel (thick lines). The stimulus onset is indicated by the grey vertical line. Peak-normalized averaged control arteriolar diameter change (black) and astrocytic  $\text{Ca}^{++}$  response (red) are superimposed in the inset.

that, under normal physiological conditions, accumulation of these vasoactive bi-products may not be sufficient to dominate CBF regulation [38]. While vasoactive metabolites may reach concentrations relevant for CBF regulation only in disease (e.g. cortical spreading depression, epileptic seizures, hypoxia) extracellular  $\text{K}^+$  may act as a dilator within its normal physiological range [93–95].  $\text{K}^+$  is released by all spiking neurons and can activate  $\text{K}_{\text{ir}}$  channels in the arteriolar smooth muscle causing hyperpolarization and relaxation (i.e. vasodilation) [95].  $\text{K}_{\text{ir}}$  channels are also present in the endothelial cells [96] and can underlie EC-mediated propagation of signalling along the vascular wall [97]. Glial role in  $\text{K}^+$  transport from the extracellular to perivascular space (known as 'K<sup>+</sup> siphoning') has also been proposed but remains controversial [98–100]. Although further studies are required to document the role of  $\text{K}_{\text{ir}}$  channels in local and conducted vasodilation *in vivo*, one or more of these  $\text{K}^+$ -mediated mechanisms may account for the residual dilation response insensitive to the blockers of molecular signalling.

Thus, although multiple vasoactive mechanisms have been identified, not all of them act at once. Rather, specific pathways are likely to be selectively involved depending on: (i) timescales, e.g. initiation and sustaining of dilation; (ii) physiological or pathological conditions, e.g. normal stimulus-induced hyperemia or CBF increase in response to a seizure; (iii) local or global/regional nature of CBF regulation; and (iv) proximity to the site of the initial dilation (locally induced or conducted responses). Under normal physiological conditions, neuronal signalling seems to play the dominant role in driving arteriolar dilation and constriction. In addition, rises in the extracellular  $\text{K}^+$  associated with neuronal firing may contribute to both local and conducted response. In disease, aberrant neuronal activity and upregulation of astrocytic  $\text{Ca}^{++}$  excitability can lead to the release of vasoactive astrocytic messengers and accumulation of vasoactive metabolites (e.g. lactate) 'taking over' the CBF control [101–103].

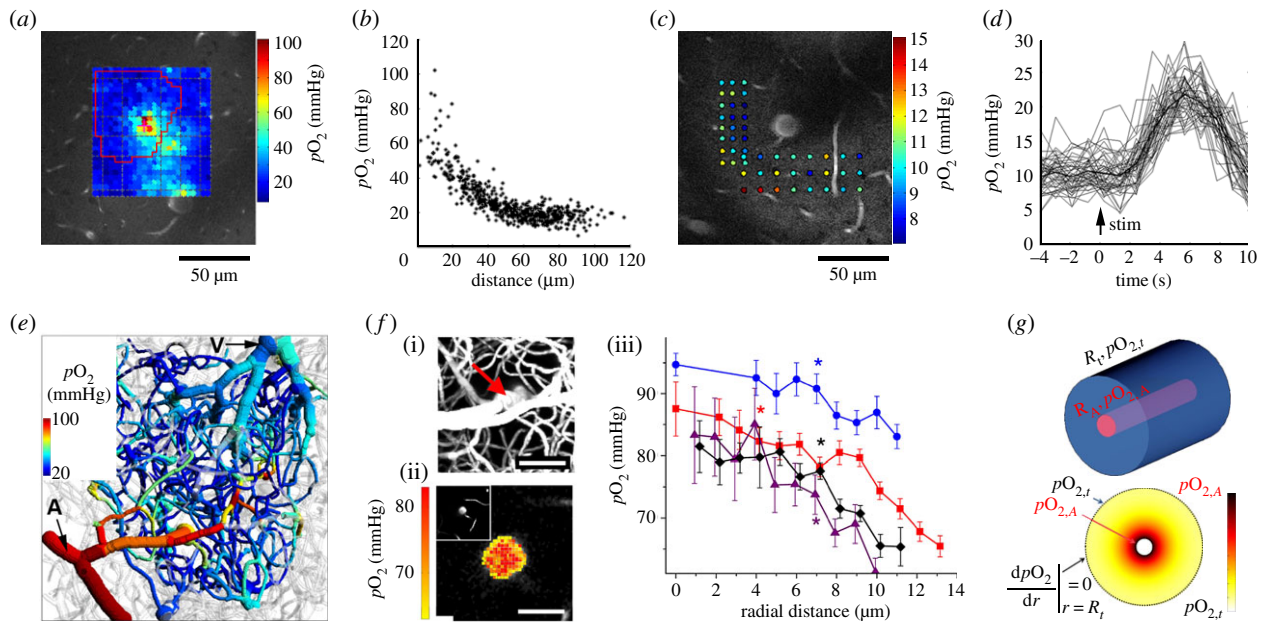


**Figure 5.** Two-photon imaging of  $pO_2$  and estimation of  $CMRO_2$ . (a) A reference vascular image with an arteriole (labelled by a magenta cross). The fluorescent contrast is due to intravascular FITC. Measured  $pO_2$  values are superimposed. The red contour indicates the segmented arteriolar territory. (b) The  $pO_2$  values from (a) plotted as a function of the radial distance from the arteriole. (c,d) Stimulus-evoked time courses of  $pO_2$  change (d) extracted from each of the measurement points in (c). The thick line shows the average. (e) Intravascular  $pO_2$  measurements overlaid over a reconstructed microvascular network connecting a diving arteriole and a neighbouring surfacing venule. (f)  $pO_2$  distribution measured inside diving arterioles. (i) MIP of a two-photon image stack. Scale bar, 50  $\mu\text{m}$ . (ii)  $pO_2$  map inside the arteriole (labelled by the red arrow in the image on top) 100  $\mu\text{m}$  below the cortical surface. Scale bar, 20  $\mu\text{m}$ . (iii) Radial intra-arteriolar  $pO_2$  profiles (radial distance calculated from the vessel axis to the vessel wall) from four diving arterioles similar to the example vessel presented on the left. (g) Schematic of the Krogh model parameters.

### 3. Microscopic $O_2$ transport and consumption

A large body of experimental studies has established the basic properties of intra- and extravascular oxygen changes during changes in neuronal activity [104–114] powering biophysical modelling of  $O_2$  transport and consumption [115–118]. Recently, our ability to measure  $O_2$  with microscopic resolution has been revolutionized by the arrival of specific optical probes excitable in the two-photon regime [119–121] and the development of two-photon phosphorescence lifetime microscopy (2PLM) [122]. 2PLM allows measurement of both intravascular and tissue-partial pressure of  $O_2$  ( $pO_2$ ) with unprecedented spatial resolution, and is well suited to imaging of  $pO_2$  changes at the baseline as well as during functional activation (figure 5a–e) [13,123–126]. 2PLM can also be used to estimate blood flow in individual capillaries simultaneously with the intracapillary  $pO_2$  [125].

2PLM offers a novel method for quantitation of  $CMRO_2$  based on  $pO_2$  gradients immediately surrounding diving arterioles (figure 5a) [13]. This method is based on the assumption that peri-arterial tissue—the area within an approximate 100  $\mu\text{m}$  radius around a diving arteriole—receives all of its  $O_2$  from the arteriole. Several properties of the cortical vasculature justify this assumption. First, two-photon imaging of the vascular architecture in the rat and mouse SI indicates the absence of capillaries around diving arterioles [127]. Second, two-photon measurements of tissue  $pO_2$  around diving arterioles show large gradients—a decrease in tissue  $pO_2$  moving away from the diving arteriole—implying significant  $O_2$  delivery from the arteriole (figure 5a,b) [13]. Third, two-photon measurements of intravascular  $pO_2$  within diving arterioles demonstrate a  $pO_2$  decrease moving from the vessel centre to the arteriolar wall indicating that  $O_2$  leaves through the arteriolar wall (figure 5f) [123]. Fourth, the intravascular

$pO_2$  of diving arterioles decreases with increasing cortical depth, again implying  $O_2$  delivery from the arteriole [123]. This last finding, originally reported under anaesthesia, was not reproduced by a recent study in awake mice [128]. This discrepancy, however, may be explained by the higher blood-flow velocity resulting in lower  $O_2$  extraction fraction. In other words, diving arterioles are likely to supply  $O_2$  also in awake mice, but produce a negligible effect on the intravascular  $pO_2$  due to high flux of red blood cells. Measurements of tissue  $pO_2$  in awake mice will be required to confirm this prediction.

Overall, this organization agrees with Krogh's model of  $O_2$  diffusion from a cylinder (figure 5g) [129] where the required condition is a single  $O_2$  source in the middle of the tissue cylinder—the diving arteriole. This model is described by the following equation:

$$pO_{2,i}(r) = pO_{2,A} + \frac{CMRO_2}{4D\alpha} (r^2 - R_A^2) - \frac{CMRO_2^2}{2D\alpha} R_i^2 \ln\left(\frac{r}{R_A}\right),$$

where  $r$  is the radial distance from the arteriolar wall,  $pO_{2,A}$  is tissue  $pO_2$  measured at the outer vessel wall boundary,  $R_A$  is vessel radius,  $D$  is tissue  $O_2$  diffusivity and  $\alpha$  is tissue  $O_2$  solubility. The Krogh model also includes an external tissue radius  $R_i$  which is estimated as the radius where  $pO_2$  gradient is zero (a fitted parameter in the calculation along with  $CMRO_2$ ). Assuming that  $CMRO_2$  is uniform for a particular cortical layer, the estimate obtained from the peri-arteriolar tissue can be treated as representative  $CMRO_2$  within a cortical column (200–300  $\mu\text{m}$  in diameter in the mouse SI). The assumption of uniform  $CMRO_2$  is based on the locally uniform distribution of neuronal and glial cells in the cortex—the absence of anatomical differences between peri-arterial spaces and other cortical regions [130]. Therefore, while at the cellular scale  $CMRO_2$  may be heterogeneous,  $CMRO_2$  based on the area

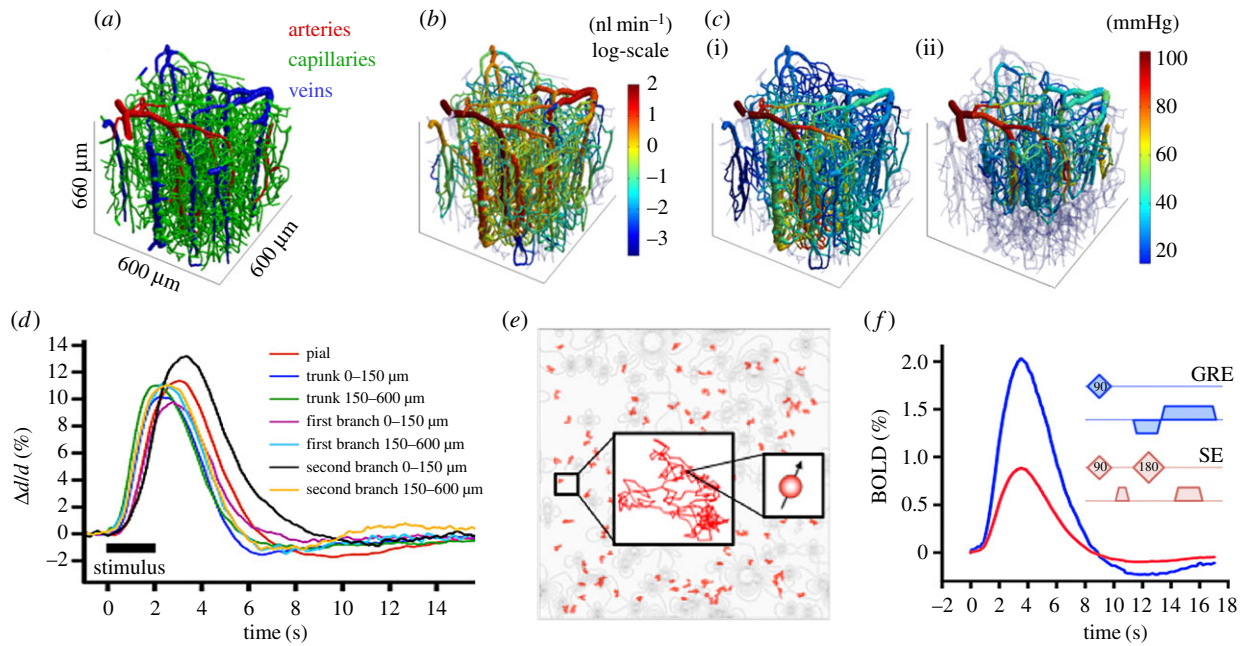


**Figure 6.** Bottom-up modelling of the haemodynamic response. (a) Reconstructed microvascular network with segmented arterioles, capillaries and venules. (b) Simulated CBF. (c) Simulated (i) and experimental (ii) measurements of  $pO_2$ . (d) Experimentally obtained dilation time courses averaged across subjects sorted by the cortical depth and branching order. (e) Simulation of nuclear spins diffusing in the magnetic field perturbation volume. (f) Time series of the simulated extravascular signals obtained with the gradient echo (GRE) and spin echo (SE) fMRI pulse sequences. The spatial gradients applied to simulate GRE and SE signals are shown in the inset.

within an approximate  $100\ \mu\text{m}$  radius around a diving arteriole should represent an accurate local estimate. The Krogh model can be extended to the dynamic regime (i.e. changes in  $\text{CMRO}_2$  induced by neuronal response to a stimulus) by considering two parallel processes: diffusion of  $O_2$  from the arteriole and consumption of  $O_2$  by tissue [131]. In the future, a combination of 2PLM with OG stimulation will allow profiling of  $O_2$  consumption associated with activity of specific neuronal cell types and across different respective levels of excitatory and inhibitory activity.

Since under normal physiological conditions neurovascular and neurometabolic coupling occur in parallel (figure 1), we must think of CBF and  $\text{CMRO}_2$  as being driven in parallel by neuronal activity, and potentially by different aspects of neuronal activity: the CBF response is determined by the dilatory and constrictive agents released from active neurons while  $\text{CMRO}_2$  response directly reflects the energetic costs (associated mainly with neuronal repolarization [39,132]).

#### 4. Bridging across spatial scales: from single-vessel dilation to macroscopic cerebral blood flow and cerebral metabolic rate of oxygen

Understanding neurovascular mechanisms requires access to concrete microscopic parameters with high-resolution, sensitivity and specificity. While such measurements are achievable in animal experiments, non-invasive imaging in humans is limited (at least, in its current practice) in resolution and, often, by the indirect nature of the measured signals. This is due to a complex relationship between the measured non-invasive signals and the underlying physiological variables (a.k.a. the ‘measurement theory’ problem). Therefore, individual microscopic measurements have

to be integrated within a computational model in order to reconstruct the phenomenon on the macroscopic scale.

One example of such a model is the vascular anatomical network (VAN) that allows a detailed, ‘bottom-up’ simulation of macroscopic CBF and  $\text{CMRO}_2$  [30–32]. This model is based on a realistic three-dimensional cortical microvascular network (e.g.  $600 \times 600 \times 600\ \mu\text{m}$  in Gagnon *et al.* [32]) populated with experimentally obtained microscopic measurements of  $pO_2$  (from 2PLM) and CBF (using optical coherence tomography). A three-dimensional microvascular angiogram can be obtained *in vivo* using two-photon microscopy followed by graphing and segmentation of the vascular network: from the pial arterioles, through the capillary network to the pial veins (figure 6a–c).  $pO_2$  distributions are then obtained by modelling  $O_2$  transport and consumption using the advection–diffusion equation [133] with the experimental data serving as boundary conditions. For simulation of activation dynamics, experimentally obtained time courses of dilation (e.g. as a function of the cortical depth and branching order) are used as the input to the VAN model for calculation of stimulus-induced changes in CBF and oxygen distribution (figure 6d).

Furthermore, the VAN model permits simulation of magnetic field perturbations as a function of specific pulse-sequence parameters to predict the fMRI signal from first principles. This is done by calculation of the microscopic distortions in the magnetic field arising from the spatio-temporal distribution of deoxygenated haemoglobin. Keeping track of changes in the intravascular deoxygenated haemoglobin, resulting from the dynamics of vasodilation and  $O_2$  consumption, one can simulate the dephasing of protons, excited by different pulse sequences, as they diffuse through the heterogeneous magnetic field (figure 6e,f). These predictions can then be contrasted against real fMRI data to ensure validity of the model [32].

Using arteriolar diameter and  $pO_2$  measurements in response to OG activation of specific neuronal cell types as the input, the VAN model can be used to estimate the macroscopic CBF and CMRO<sub>2</sub> effects driven by the individual neuronal populations.

## 5. Bridging across spatial scales: from activity of specific neuronal cell types to macroscopic current dipole

The need to bridge between the micro- and macroscopic scale also applies to non-invasive measurements of neuronal electrical activity obtained with MEG or EEG that reflect the same physical process but differ in their relative sensitivity to current dipoles depending on their orientation and depth [134]. The MEG/EEG signals are dominated by intracellular currents flowing up and down the cortical column along cortical PCs [135]. This is because in cerebral cortex PCs are aligned along the depth axis forming a preferred orientation for the current flow that can be captured from distance as the current dipole moment. Other cell types lack a preferred orientation (e.g. excitatory stellate cells or parvalbumin-positive inhibitory basket cells) and/or are present in small numbers (e.g. bipolar inhibitory neurons) compared with PCs [136] such that their contribution to the MEG/EEG signal is expected to be negligible.

Localization of current dipole from MEG/EEG data is a difficult problem that has been addressed by many groups using experimental and computational methods [9,135,137]. In the absence of additional priors, this problem is ill-posed. In the SI, however, the location of neuronal activity is known due to somatotopic maps. These maps can be validated/refined for each subject using fMRI. Thus, we can obtain locations of cortical signal generators from fMRI and get accurate estimation of the time course of neuronal activity from EEG/MEG [10,138].

The dipole moment can be forward-calculated using depth-resolved (laminar) extracellular recordings of Local Field Potential (LFP) [139]. The laminar LFP profiles can be used to obtain laminar Current Source Density (CSD) [140]. Then, the dipole moment is computed as the moment of the current sources and sinks along the cortical depth [141,142] (figure 7*a,b*). To generate a measurable dipole, synaptic inputs have to arrive either at the top of PC dendritic tree (apical dendrites) or at the bottom (the soma and basal dendrites) [150,151]. Inputs covering the entire length of a PC or those arriving exactly at the middle would not generate a dipole. Fortunately, synaptic projections (i.e. projection 'domains') from at least some types of inhibitory neurons onto PCs segregate along the depth axis (figure 7*c*) [143,152]. For example, somatostatin-positive Martinotti cells synapse on the apical dendrites [153] while double bouquet cells positive for neuronal nitric oxide synthase synapse at the basal dendrites [143]. These different patterns of synaptic projections onto PCs are expected to produce distinguishable laminar LFP profiles, and some of these differences will survive in the corresponding current dipole. For this reason, MEG/EEG signals can offer additional constraints for the interpretation of fMRI data in terms of activity of neuronal cell-type-specific populations. As such, different types of inhibitory neurons may produce constriction (such as NPY), dilation, or have no vasoactive effect. However, even when multiple types of inhibitory neurons

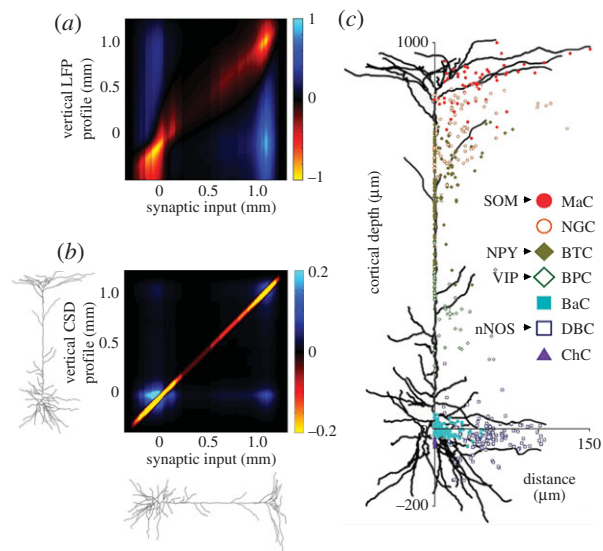


**Figure 7.** Synaptic projection domains in the generation of LFP and CSD. (*a,b*) Predicted LFP and CSD profiles for a population of layer 5 PC due to synaptic inputs. The vertical axis shows the depth profile as a function of the vertical position of synaptic inputs (the horizontal axis). The profiles are analogous to the plots in fig. 13*a* in [142], but here the cortical surface is assumed to be covered with highly conductive saline. (*c*) Inhibitory projection domains of different types of inhibitory neurons to layer V PC. The scatter plot showing the horizontal and vertical distance of the synapses made by seven groups of layer II/III inhibitory neurons from the soma of layer V PC is reproduced with permission from [143]. The plot is overlaid on an example layer V PC morphology obtained from NeuroMorpho.org [144] (ID = 070123-z1). The indicated correlation between morphological classification of the inhibitory neurons and expression of neuropeptides and NO is based on the authors' interpretation of [41,136,145–149].

have the same vasodilatory effect, they may differ in the laminar profile of their synaptic projection domains onto PCs resulting in distinct contributions to the current dipole.

Thus, the idea would be to build a library of the laminar LFP profiles due to OG stimulation of specific neuronal cell types (e.g. Martinotti cells). The reason for using OG stimulation would not be to reproduce natural or balanced neuronal activity patterns. Rather, the goal is to produce artificially selective activation of specific neuronal populations for isolation of their electrical (as well as vasoactive and metabolic) effects. A natural laminar LFP profile (or the current dipole)—such as that induced by a sensory stimulus in an intact cortical neuronal circuit—can then be viewed as a weighted linear superposition of these population-specific 'primitives' (due to the linear superposition nature of electromagnetic signals [10,138,139]).

Experimental estimation of these primitives requires selective activation of a specific population of presynaptic neurons, which can be achieved using optogenetics. A combination of OG activation of a presynaptic population  $j$  with the laminar LFP recordings would provide a CSD profile resulting from currents in all PCs postsynaptic to  $j$ . To obtain CSD profiles specific to a particular population of PCs (those with the cell body located in layer II/III, layer V or layer VI), one can employ computational decomposition methods [142,154]. Furthermore, detailed 'realistic' models of cortical columns have recently become available due to a decade-long effort by The Blue Brain Project currently continuing under the umbrella of The Human Brain Project. These models of synaptically connected spiking neurons with realistic morphologies can be combined with the physical principles governing generation

of LFP [155,156] for prediction of LFP/CSD/dipole signals resulting from complex circuit phenomena. These models also allow testing for potential non-additive effects resulting from active conductances (e.g. the  $\text{Ca}^{++}$  spike in PCs [157]).

Given experimentally derived knowledge on the vasoactive role and energetic costs of activity for the individual cell-type-specific neuronal populations, we may be able to use neuronal network models to predict CBF and  $\text{CMRO}_2$  changes associated with specific circuit activity patterns. Translation to macroscopic fMRI signals, however, would still require models like VAN that take into account vascular structure and the MRI measurement theory, such as sensitivity of the fMRI signal to specific vascular compartments or orientation of the main magnetic field relative to blood vessels.

## 6. Estimation of cell-type-specific neuronal activity from macroscopic cerebral blood flow, cerebral metabolic rate of oxygen and current dipole

Let us assume we had experimentally established cell-type-specific time courses of vascular diameter changes, microscopic  $p\text{O}_2/\text{CMRO}_2$  and the laminar LFP/CSD profile. Let us further assume that we used these data to simulate corresponding macroscopic physiological parameters. Assuming a linear superposition of the effects, natural stimulus-induced responses can then be expressed as follows:

$$\Delta F(t) = \sum_j W_{fj}(t) \otimes \Delta S_j(t), \quad (6.1)$$

$$\Delta C(t) = \sum_j W_{cj}(t) \otimes \Delta S_j(t) \quad (6.2)$$

$$\text{and } \Delta D(t) = \sum_j W_{dj}(t) \otimes \Delta S_j(t), \quad (6.3)$$

where  $\Delta F(t)$ ,  $\Delta C(t)$  and  $\Delta D(t)$  are the observed macroscopic CBF,  $\text{CMRO}_2$  and the current dipole moment, respectively;  $W_{fj}(t)$ ,  $W_{cj}(t)$  and  $W_{dj}(t)$  are weighting factors per unit activity for neuronal population of cell type  $j$ ;  $\Delta S_j(t)$  is the amplitude of neuronal activity for the population  $j$  and  $\otimes$  represents a temporal convolution.

As the release of vasoactive signalling molecules (and  $\text{K}^+$ ) in neurons normally requires spike-induced depolarization, we think of  $\Delta S_j(t)$  as the cell-type-specific spiking response. This should not be interpreted as settling the classical question of whether spiking or synaptic activity correlates better with BOLD in favour of spiking. Historically, this question was motivated by the idea of a metabolic feedback. This idea postulated that CBF increase was mechanistically driven by the accumulation of vasoactive energy metabolites [92]. In our view, on the other hand, neurovascular coupling under normal conditions is governed by a feed forward mechanism, where specific vasoactive signalling agents released by active neurons drive dilation and constriction, depending on the cell type.

For CBF and  $\text{CMRO}_2$ ,  $\Delta S_j(t)$  in equations (6.1) and (6.2) can be approximated as a delta function locked to an individual neuronal event (as long as neuronal events are brief on the haemodynamic timescale) and  $W_j(t) \otimes \Delta S_j(t)$ —as a scaled cell-type-specific impulse response function. Electrophysiological signals, by contrast, are measured on the actual temporal scale of neuronal activity. Therefore, for  $\Delta D(t)$  (equation (6.3)),  $\Delta S_j(t)$  represents a time course of spiking activity for the cell type  $j$ . As  $\Delta S_j(t)$  in equation (6.3) stands for spiking and  $\Delta D(t)$  reflects currents (flowing up and down

PC dendrites), the cell-type-specific weighting factor  $W_{dj}(t)$  can be thought of as the transfer function from the presynaptic spikes in cell type  $j$  to postsynaptic currents in PCs. As some of us described previously [142], cell-type-specific laminar CSD can be expressed as the presynaptic spiking activity convolved with an exponential function representing the resulting postsynaptic currents in PCs. Therefore,  $W_{dj}(t)$  represent the dipole moment of these postsynaptic currents. Finally, the formalism described in equations (6.1)–(6.3) is based on the assumption of linearity. The validity of this assumption can be evaluated experimentally by performing direct measurements of  $\Delta S_j(t)$  in response to the sensory stimulus (e.g. using cell-type-specific expression of genetically encoded  $\text{Ca}^{++}$  probes) and comparing the measured and estimated  $\Delta S_j(t)$  across stimulus conditions.

In the simplest case of two considered cell types—excitatory and inhibitory—we would have only two unknowns:  $\Delta S_j$  for excitation and inhibition. Based on our recent study attributing vasoconstriction *in vivo* to activation of NPY-positive inhibitory neurons (figure 3) [63], we predict that  $W_j(t)$  for excitatory and inhibitory neurons will integrate to a positive and negative number, respectively. Therefore, at steady state ('blocked' experimental design), we would obtain positive  $\Delta F$  (an increase in CBF) for excitation and negative  $\Delta F$  (a decrease in CBF) for inhibition. This would be consistent with vasoconstriction and negative BOLD previously observed by us and others in the ipsilateral hemisphere experiencing transcallosal inhibition [29,38,50,53]. For  $\Delta C$ , we expect a smaller increase in  $\Delta \text{CMRO}_2$  due to activity of inhibitory neurons compared with excitatory neurons [39,132]. However, inhibition can suppress excitatory activity below the baseline resulting in net negative  $\Delta \text{CMRO}_2$ , and experimental studies combining 2PLM with controlled manipulation of neuronal circuits will be required to evaluate the net  $\Delta \text{CMRO}_2$  across different respective levels of excitation and inhibition.

## 7. Human translation

In the previous section, we were discussing the problem of estimation of neuronal activity given macroscopic CBF,  $\text{CMRO}_2$  and current dipole. For human translation, a separate and equally important problem is how to reliably estimate these macroscopic physiological parameters from non-invasive measurements. This problem is particularly severe for  $\text{CMRO}_2$  requiring two different types of measurements—BOLD and ASL—plus a calibration step [17–19] (CBF can be extracted from ASL using well-tested methods [158–160]; estimation of current dipole moment with MEG/EEG is also straightforward as long as the location of neuronal activity and cortical orientation is known [161]). In current practice,  $\text{CMRO}_2$  in human imaging studies is estimated using simplified, macroscopic models that fit the fMRI response by assuming a specific functional form for the relationship between the spatially averaged, or 'lumped', physiological parameters of interest and the macroscopic imaging signals [17,162,163]. One specific example is the Davis model that was originally derived from simplified physiological assumptions to estimate relative changes in  $\text{CMRO}_2$  from calibrated BOLD measurements [17] (ASL provides a direct measurement of CBF; no modelling is required). However, such  $\text{CMRO}_2$  estimates have never been validated against direct measurements of the physiological parameters in question.

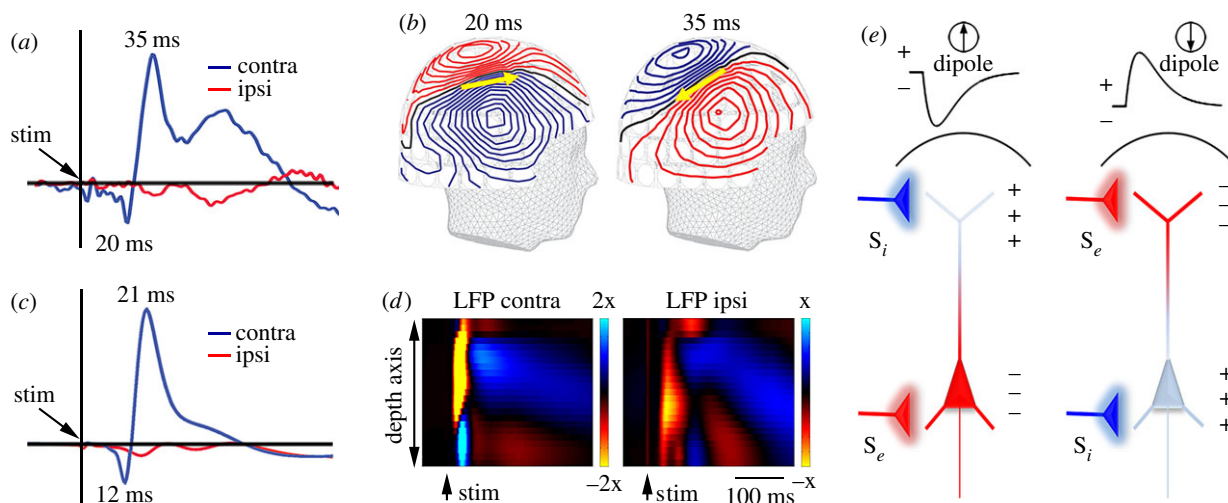


**Figure 8.** The current dipole moment in mice and humans. *(a,b)* Human MEG measurements in response to the median nerve stimulation: cortically constrained source estimate [10] (current dipole) for the SI ROI *(a)* and the corresponding SEF contour plot *(b)*. *(c,d)* Rat dipole waveform *(c)* calculated from laminar LFP *(d)* in response to weak electrical forepaw stimulation. Contra, contralateral stimulus; ipsi, ipsilateral stimulus. *(e)* Schematic of the current dipole and surface potential signals due to excitatory ( $S_e$ ) and inhibitory ( $S_i$ ) inputs.

Bottom-up simulators of the fMRI signals can provide the ground truth for validation of these simplified macroscopic models. The first study of this kind is that by Gagnon *et al.* [164]. Gagnon *et al.* used the VAN model, based on the fundamental physiological processes with a microscopic level of detail, to simulate BOLD and ASL signals bottom-up. The simulated BOLD and ASL signals provided the input into the Davis model for estimation of the CMRO<sub>2</sub> change. This estimate was then compared to the true CMRO<sub>2</sub> known from VAN. The results revealed that to get a valid CMRO<sub>2</sub> estimate, the free parameters of the Davis model (known as  $\alpha$  and  $\beta$ ) had to assume values inconsistent with the physiological effects they were originally introduced to represent. The obvious limitation here is that if any of these parameters require adjustment to fit the data under certain conditions (e.g. in disease or ageing) this adjustment cannot be interpreted in terms of the underlying physiology.

In the future, calibration against large-scale realistic simulations where both the micro- and macroscopic reality is known will be essential for arriving at macroscopic models that would provide accurate estimation of CMRO<sub>2</sub> with model parameters derived from valid physiological assumptions. Ultimately, we would need to come up with a Davis-like formalism with a few model parameters. However, more detailed analytical models (still simplified compared to VAN), such as the one recently developed by Griffith & Buxton [165], may be very useful as an intermediate step. In contrast to VAN, which gives only the empirical relationship, the Griffith *et al.* [15] model analytically captures the results of the bottom-up, microscopic simulation and thus can be used to study a mathematical relationship between interpretable parameters. Eventually, models like that in Griffith *et al.* [15] would need to be reduced to obtain a simpler top-down, Davis-like formalism applicable to human fMRI experiments.

## 8. Neuronal circuits in mice and humans

The principle of leveraging mechanistic neurovascular/neurometabolic insights obtained in animals for physiological underpinning of human data relies on the assumption of

similar/comparable neuronal network activity. What are the reasons to believe that this assumption is valid? Figure 8 shows an example Somatosensory Evoked Field (SEF) response to the median nerve stimulation in a normal human subject obtained with MEG (figure 8*a,b*) and the equivalent current dipole moment calculated from laminar LFP in response to forepaw stimulation in an anaesthetized rat (figure 8*c,d*). These dipole time courses are remarkably similar, indicating similar patterns of evoked neuronal circuit activity in the rodent and human SI. For example, in both cases the response to the contralateral stimulus is composed of the initial negative peak followed by a positive one. These peaks occur earlier in the rat (12/21 ms) compared to the human (20/35 ms) due to differences in the distance that neuronal impulses have to travel. The human SEF has a secondary positive peak that is less pronounced in the rat; this difference may be attributed to anaesthesia. Thus, at least in the SI, the basic circuit function is preserved from rodents to humans, although physical scaling laws would need to be applied to account for systematic differences (e.g. longer electrical conduction times in humans). That being said, specific differences between these two species have been documented, including neuronal and astrocytic morphology and function and long-range connectivity [166–168], and should be considered while translating model parameters from mouse to human.

Translation from the micro- to macroscopic scale inevitably results in loss of information, and activation of some cell-type-specific neuronal populations would have similar signatures in the macroscopic observables. The multimodal imaging approach aims to overcome this fundamental degeneracy of macroscopic measurements, as much as possible, by a combination of measurements. For example, inhibitory inputs to the top (apical) dendrites of PCs produce the same polarity of the macroscopic current dipole (and of the surface potential) as excitatory inputs to the basal dendrites (figure 8*e*). Likewise, excitatory inputs to the top cannot be distinguished from inhibitory inputs to the bottom. However, only inhibitory activity produces vasoconstriction [63] (figure 3). Therefore, a combination of the current dipole and CBF response can disambiguate between these possibilities.

## 9. Conclusion

How can we explicitly estimate the cellular level of neuronal functional organization in humans where we do not have access to microscopic measurements of any kind? All that we have is non-invasive measurements that can be thought of as ‘observations from a distance’ of signals with indirect relationship to the parameters of interest—neuronal activity at the level of specific cell types. In this essay, we argued that the activation of different neuronal cell types has different signatures in the evoked CBF, CMRO<sub>2</sub> and the macroscopic current dipole responses, and that by measuring these responses non-invasively in the human brain we will be able to probe more deeply the underlying neuronal circuit activity. We sketched a path for estimation of cell-type-specific neuronal activity from non-invasive measurements that begins with identification of the vasoactive role, energetic costs and extracellular electrical potentials/currents associated with activity of specific neuronal cell types. These types of experiments require experimental tools for microscopic measurement and manipulation that are only available in model organisms. These data are needed to simulate non-invasive measurements bottom-up and build a comprehensive multiscale forward model connecting the dots between neuronal activity at the level of

specific cell types to fMRI and MEG/EEG observables. For inference of neuronal activity in humans, this forward model would need to be combined with a set of non-invasive experimental measurements in a Bayesian approach [33]. Following this path may lead to a paradigm shift in human fMRI studies: from a simple mapping of fMRI signal change to the explicit estimation of the respective activity levels of specific neuronal cell types, providing a bridge between a large body of cellular and circuit-level neuroscience knowledge achieved in animals and the human ‘measurables’ and opening the door for human hypothesis-driven experiments that are currently unfeasible.

**Competing interests.** The authors declare no conflict of interests.

**Funding.** We gratefully acknowledge support from the UCSD Center for Brain Activity Mapping (CBAM), NIH (NS057198, EB00790, AG042026 and S10RR029050), the Research Council of Norway, and the Ministry of Education, Youth and Sports of the Czech Republic (project CEITEC 2020 (LQ1601)). K.K. was supported by a postdoctoral fellowship from the International Headache Society in 2014 and TUBITAK in 2015. M.T. and M.D. were supported by postdoctoral fellowships from the German Research Council (DFG TH 2031/1) and Natural Sciences and Engineering Research Council of Canada, respectively.

**Acknowledgements.** We thank Christopher G.L. Ferri for his careful and critical reading of the manuscript.

## References

- Valdes-Sosa PA, Roebroeck A, Daunizeau J, Friston K. 2011 Effective connectivity: influence, causality and biophysical modeling. *Neuroimage* **58**, 339–361. (doi:10.1016/j.neuroimage.2011.03.058)
- Buxton RB. 2010 Interpreting oxygenation-based neuroimaging signals: the importance and the challenge of understanding brain oxygen metabolism. *Front. Neuroenerget.* **2**, 8. (doi:10.3389/fnene.2010.00008)
- Logothetis NK. 2002 The neural basis of the blood-oxygen-level-dependent functional magnetic resonance imaging signal. *Phil. Trans. R. Soc. Lond. B* **357**, 1003–1037. (doi:10.1098/rstb.2002.1114)
- Kim S-G, Ogawa S. 2012 Biophysical and physiological origins of blood oxygenation level-dependent fMRI signals. *J. Cereb. Blood Flow. Metab.* **32**, 1188–1206. (doi:10.1038/jcbfm.2012.23)
- Vanzetta I, Grinvald A. 2008 Coupling between neuronal activity and microcirculation: implications for functional brain imaging. *Hfsp J.* **2**, 79–98. (doi:10.2976/1.2889618)
- Harel N, Bolan PJ, Turner R, Ugurbil K, Yacoub E. 2010 Recent advances in high-resolution MR application and its implications for neurovascular coupling research. *Front. Neuroenerget.* **2**, 130. (doi:10.3389/fnene.2010.00130)
- Ogawa S, Tank DW, Menon R, Ellermann JM, Kim SG, Merkle H, Ugurbil K. 1992 Intrinsic signal changes accompanying sensory stimulation: functional brain mapping with magnetic resonance imaging. *Proc. Natl Acad. Sci. USA* **89**, 5951–5955. (doi:10.1073/pnas.89.13.5951)
- Kwong KK *et al.* 1992 Dynamic magnetic resonance imaging of human brain activity during primary sensory stimulation. *Proc. Natl Acad. Sci. USA* **89**, 5675–5679. (doi:10.1073/pnas.89.12.5675)
- Rosa MJ, Daunizeau J, Friston KJ. 2010 EEG-fMRI integration: a critical review of biophysical modeling and data analysis approaches. *J. Integr. Neurosci.* **9**, 453–476. (doi:10.1142/S0219635210002512)
- Dale AM, Liu AK, Fischl BR, Buckner RL, Belliveau JW, Lewine JD, Halgren E. 2000 Dynamic statistical parametric mapping: combining fMRI and MEG for high-resolution imaging of cortical activity. *Neuron* **26**, 55–67. (doi:10.1016/S0896-6273(00)81138-1)
- Leithner C, Royl G. 2014 The oxygen paradox of neurovascular coupling. *J. Cereb. Blood Flow Metab.* **34**, 19–29. (doi:10.1038/jcbfm.2013.181)
- Buxton RB. 2013 The physics of functional magnetic resonance imaging (fMRI). *Rep. Progress Phys. Phys. Soc.* **76**, 096601. (doi:10.1088/0034-4885/76/9/096601)
- Devor A *et al.* 2011 ‘Overshoot’ of O<sub>2</sub> is required to maintain baseline tissue oxygenation at locations distal to blood vessels. *J. Neurosci.* **31**, 13 676–13 681. (doi:10.1523/JNEUROSCI.1968-11.2011)
- Buxton RB, Griffeth VE, Simon AB, Moradi F, Shmuel. 2014 Variability of the coupling of blood flow and oxygen metabolism responses in the brain: a problem for interpreting BOLD studies but potentially a new window on the underlying neural activity. *Front. Neurosci.* **8**, 139. (doi:10.3389/fnins.2014.00139)
- Griffeth VE, Perthen JE, Buxton RB. 2011 Prospects for quantitative fMRI: investigating the effects of caffeine on baseline oxygen metabolism and the response to a visual stimulus in humans. *Neuroimage* **57**, 809–816. (doi:10.1016/j.neuroimage.2011.04.064)
- Friston KJ. 2009 Modalities, modes, and models in functional neuroimaging. *Science* **326**, 399–403. (doi:10.1126/science.1174521)
- Davis TL, Kwong KK, Weisskoff RM, Rosen BR. 1998 Calibrated functional MRI: mapping the dynamics of oxidative metabolism. *Proc. Natl Acad. Sci. USA* **95**, 1834–1839. (doi:10.1073/pnas.95.4.1834)
- Hoge RD. 2012 Calibrated FMRI. *Neuroimage* **62**, 930–937. (doi:10.1016/j.neuroimage.2012.02.022)
- Pike GB. 2012 Quantitative functional MRI: concepts, issues and future challenges. *Neuroimage* **62**, 1234–1240. (doi:10.1016/j.neuroimage.2011.10.046)
- Bargmann CI, Marder E. 2013 From the connectome to brain function. *Nat. Methods* **10**, 483–490. (doi:10.1038/nmeth.2451)
- Insel TR, Landis SC, Collins FS. 2013 Research priorities. The NIH BRAIN Initiative. *Science* **340**, 687–688. (doi:10.1126/science.1239276)
- Devor A *et al.* 2013 The challenge of connecting the dots in the B.R.A.I.N. *Neuron* **80**, 270–274. (doi:10.1016/j.neuron.2013.09.008)
- Markram H. 2012 The human brain project. *Sci. Am.* **306**, 50–55. (doi:10.1038/scientificamerican0612-50)
- Simons DJ, Carvell GE. 1989 Thalamocortical response transformation in the rat vibrissa/barrel system. *J. Neurophysiol.* **61**, 311–330.
- Kleinfeld D, Delaney KR. 1996 Distributed representation of vibrissa movement in the upper layers of somatosensory cortex revealed with voltage-sensitive dyes. *J. Comp. Neurol.* **375**, 89–108. (doi:10.1002/(SICI)1096-9861(19961104)375:1<89::AID-CNE6>3.0.CO;2-K)

26. Takashima I, Kajiwara R, Iijima T. 2001 Voltage-sensitive dye versus intrinsic signal optical imaging: comparison of optically determined functional maps from rat barrel cortex. *Neuroreport* **12**, 2889–2894. (doi:10.1097/00001756-200109170-00027)
27. Derdikman D, Hildesheim R, Ahissar E, Arieli A, Grinvald A. 2003 Imaging spatiotemporal dynamics of surround inhibition in the barrels somatosensory cortex. *J. Neurosci.* **23**, 3100–3105.
28. Ferbert A, Priori A, Rothwell JC, Day BL, Colebatch JG, Marsden CD. 1992 Interhemispheric inhibition of the human motor cortex. *J. Physiol.* **453**, 525–546. (doi:10.1113/jphysiol.1992.sp019243)
29. Hlushchuk Y, Hari R. 2006 Transient suppression of ipsilateral primary somatosensory cortex during tactile finger stimulation. *J. Neurosci.* **26**, 5819–5824. (doi:10.1523/JNEUROSCI.5536-05.2006)
30. Boas DA, Jones SR, Devor A, Huppert TJ, Dale AM. 2008 A vascular anatomical network model of the spatio-temporal response to brain activation. *Neuroimage* **40**, 1116–1129. (doi:10.1016/j.neuroimage.2007.12.061)
31. Fang Q, Sakadžić S, Ruvinskaya L, Devor A, Dale AM, Boas DA. 2008 Oxygen advection and diffusion in a three-dimensional vascular anatomical network. *Opt. Express* **16**, 17 530–17 541. (doi:10.1364/OE.16.017530)
32. Gagnon L *et al.* 2015 Quantifying the microvascular origin of BOLD-fMRI from first principles with two-photon microscopy and an oxygen-sensitive nanoprobe. *J. Neurosci.* **35**, 3663–3675. (doi:10.1523/JNEUROSCI.3555-14.2015)
33. Friston KJ. 2005 Models of brain function in neuroimaging. *Annu. Rev. Psychol.* **56**, 57–87. (doi:10.1146/annurev.psych.56.091103.070311)
34. Lindauer U *et al.* 2010 Neurovascular coupling in rat brain operates independent of hemoglobin deoxygenation. *J. Cereb. Blood Flow Metab.* **30**, 757–768. (doi:10.1038/jcbfm.2009.259)
35. Devor A, Boas D, Einevoll GT, Buxton RB, Dale AM. 2012 Neuronal basis of non-invasive functional imaging: from microscopic neurovascular dynamics to BOLD fMRI. In *Neural metabolism in vivo* (eds I-Y Choi, R Gruetter), pp. 433–500. Berlin, Germany: Springer.
36. Devor A *et al.* 2012 Frontiers in optical imaging of cerebral blood flow and metabolism. *J. Cereb. Blood Flow Metab.* **32**, 1259–1276. (doi:10.1038/jcbfm.2011.195)
37. Attwell D, Buchan AM, Charkop S, Lauritzen M, Macvicar BA, Newman EA. 2010 Glial and neuronal control of brain blood flow. *Nature* **468**, 232–243. (doi:10.1038/nature09613)
38. Devor A *et al.* 2008 Stimulus-induced changes in blood flow and 2-deoxyglucose uptake dissociate in ipsilateral somatosensory cortex. *J. Neurosci.* **28**, 14 347–14 357. (doi:10.1523/JNEUROSCI.4307-08.2008)
39. Attwell D, Iadecola C. 2002 The neural basis of functional brain imaging signals. *Trends Neurosci* **25**, 621–625. (doi:10.1016/S0166-2236(02)02264-6)
40. Cauli B, Hamel E. 2010 Revisiting the role of neurons in neurovascular coupling. *Front Neuroenergetics* **2**, 9. (doi:10.3389/fnene.2010.00009)
41. Cauli B, Tong XK, Rancillac A, Serluca N, Lambolez B, Rossier J, Hamel E. 2004 Cortical GABA interneurons in neurovascular coupling: relays for subcortical vasoactive pathways. *J. Neurosci.* **24**, 8940–8949. (doi:10.1523/JNEUROSCI.3065-04.2004)
42. Kocharyan A, Fernandes P, Tong XK, Vaucher E, Hamel E. 2008 Specific subtypes of cortical GABA interneurons contribute to the neurovascular coupling response to basal forebrain stimulation. *J. Cereb. Blood Flow Metab.* **28**, 221–231. (doi:10.1038/sj.jcbfm.9600558)
43. Lacroix A *et al.* 2015 COX-2-derived prostaglandin E2 produced by pyramidal neurons contributes to neurovascular coupling in the rodent cerebral cortex. *J. Neurosci.* **35**, 11 791–11 810. (doi:10.1523/JNEUROSCI.0651-15.2015)
44. Lecrux C *et al.* 2011 Pyramidal neurons are ‘neurogenic hubs’ in the neurovascular coupling response to whisker stimulation. *J. Neurosci.* **31**, 9836–9847. (doi:10.1523/JNEUROSCI.4943-10.2011)
45. Rancillac A, Rossier J, Guille M, Tong XK, Geoffroy H, Amatore C, Arbault S, Hamel E, Cauli B. 2006 Glutamatergic control of microvascular tone by distinct GABA neurons in the cerebellum. *J. Neurosci.* **26**, 6997–7006. (doi:10.1523/JNEUROSCI.5515-05.2006)
46. Shmuel A, Augath M, Oeltermann A, Logothetis NK. 2006 Negative functional MRI response correlates with decreases in neuronal activity in monkey visual area V1. *Nat. Neurosci.* **9**, 569–577. (doi:10.1038/nn1675)
47. Devor A *et al.* 2007 Suppressed neuronal activity and concurrent arteriolar vasoconstriction may explain negative blood oxygenation level-dependent signal. *J. Neurosci.* **27**, 4452–4459. (doi:10.1523/JNEUROSCI.0134-07.2007)
48. Hillman EM, Devor A, Bouchard MB, Dunn AK, Krauss GW, Skoch J, Bacskaï BJ, Dale AM, Boas DA. 2007 Depth-resolved optical imaging and microscopy of vascular compartment dynamics during somatosensory stimulation. *Neuroimage* **35**, 89–104. (doi:10.1016/j.neuroimage.2006.11.032)
49. Tian P, Teng IC, Dale AM, Devor A. 2008 Characterization of the spatiotemporal responses of surface and penetrating cerebral arterioles using two-photon microscopy. Program No. 286.5. Neuroscience Meeting Planner. Washington, DC: Society for Neuroscience. Online. ([https://neurosciences.ucsd.edu/images/nil/Website\\_2\\_28\\_2011/abstracts\\_posters/2008/PeifangSFN08\\_poster.pdf](https://neurosciences.ucsd.edu/images/nil/Website_2_28_2011/abstracts_posters/2008/PeifangSFN08_poster.pdf))
50. Alonso BD, Lowe AS, Dear JP, Lee KC, Williams SC, Finnerty GT. 2007 Sensory inputs from whisking movements modify cortical whisker maps visualized with functional magnetic resonance imaging. *Cereb. Cortex* **18**, 1314–1325. (doi:10.1093/cercor/bhm163)
51. Bressler D, Spotswood N, Whitney D. 2007 Negative BOLD fMRI response in the visual cortex carries precise stimulus-specific information. *PLoS ONE* **2**, e410. (doi:10.1371/journal.pone.0000410)
52. Kastrop A, Baudewig J, Schnaudigel S, Huonker R, Becker L, Sohns JM, Dechent P, Klingner C, Witte OW. 2008 Behavioral correlates of negative BOLD signal changes in the primary somatosensory cortex. *Neuroimage* **41**, 1364–1371. (doi:10.1016/j.neuroimage.2008.03.049)
53. Mullinger KJ, Mayhew SD, Bagshaw AP, Bowtell R, Francis ST. 2014 Evidence that the negative BOLD response is neuronal in origin: a simultaneous EEG-BOLD-CBF study in humans. *Neuroimage* **94**, 263–274. (doi:10.1016/j.neuroimage.2014.02.029)
54. Smith AT, Williams AL, Singh KD. 2004 Negative BOLD in the visual cortex: evidence against blood stealing. *Hum. Brain Mapp.* **21**, 213–220. (doi:10.1002/hbm.20017)
55. Dietrich HH, Kajita Y, Dacey Jr, RG. 1996 Local and conducted vasomotor responses in isolated rat cerebral arterioles. *Am. J. Physiol.* **271**, H1109–H1116.
56. Gustafsson F, Holstein-Rathlou N. 1999 Conducted vasomotor responses in arterioles: characteristics, mechanisms and physiological significance. *Acta Physiol. Scand.* **167**, 11–21. (doi:10.1046/j.1365-201x.1999.00582.x)
57. Segal SS, Duling BR. 1986 Flow control among microvessels coordinated by intercellular conduction. *Science* **234**, 868–870. (doi:10.1126/science.3775368)
58. Welsh DG, Segal SS. 1998 Endothelial and smooth muscle cell conduction in arterioles controlling blood flow. *Am. J. Physiol.* **274**, H178–H186.
59. Tian P *et al.* 2010 Cortical depth-specific microvascular dilation underlies laminar differences in blood oxygenation level-dependent functional MRI signal. *Proc. Natl Acad. Sci. USA* **107**, 15 246–15 251. (doi:10.1073/pnas.1006735107)
60. Nizar K *et al.* 2013 *In vivo* stimulus-induced vasodilation occurs without IP<sub>3</sub> receptor activation and may precede astrocytic calcium increase. *J. Neurosci.* **33**, 8411–8422. (doi:10.1523/JNEUROSCI.3285-12.2013)
61. Lindvere L, Janik R, Dorr A, Chartash D, Sahota B, Sled JG, Stefanovic B. 2013 Cerebral microvascular network geometry changes in response to functional stimulation. *Neuroimage* **71**, 248–259. (doi:10.1016/j.neuroimage.2013.01.011)
62. Hall CN *et al.* 2014 Capillary pericytes regulate cerebral blood flow in health and disease. *Nature* **508**, 55–60. (doi:10.1038/nature13165)
63. Uhlirva H *et al.* 2016 Cell type specificity of neurovascular coupling in cerebral cortex. *eLife* **5**, e14315. (doi:10.7554/eLife.14315)
64. Siero JC, Petridou N, Hoogduin H, Luijten PR, Ramsey NF. 2011 Cortical depth-dependent temporal dynamics of the BOLD response in the human brain. *J. Cereb. Blood Flow Metab.* **31**, 1999–2008. (doi:10.1038/jcbfm.2011.57)
65. Yu X, Qian C, Chen DY, Dodd SJ, Koretsky AP. 2014 Deciphering laminar-specific neural inputs with line-scanning fMRI. *Nat. Methods* **11**, 55–58. (doi:10.1038/nmeth.2730)
66. Hill RA, Tong L, Yuan P, Murikinati S, Gupta S, Grutzendler J. 2015 Regional blood flow in the

- normal and ischemic brain is controlled by arteriolar smooth muscle cell contractility and not by capillary pericytes. *Neuron* **87**, 95–110. (doi:10.1016/j.neuron.2015.06.001)
67. Hartmann DA, Underly RG, Grant RI, Watson AN, Lindner V, Shih AY. 2015 Pericyte structure and distribution in the cerebral cortex revealed by high-resolution imaging of transgenic mice. *Neurophotonics* **2**, 041402. (doi:10.1117/1.NPh.2.4.041402)
68. Attwell D, Mishra A, Hall CN, O'Farrell FM, Dalkara T. 2016 What is a pericyte? *J. Cereb. Blood Flow Metab.* **36**, 451–455. (doi:10.1177/0271678X15610340)
69. Drew PJ, Shih AY, Kleinfeld D. 2011 Fluctuating and sensory-induced vasodynamics in rodent cortex extend arteriole capacity. *Proc. Natl Acad. Sci. USA* **108**, 8473–8478. (doi:10.1073/pnas.1100428108)
70. Yizhar O, Fenno LE, Davidson TJ, Mogri M, Deisseroth K. 2011 Optogenetics in neural systems. *Neuron* **71**, 9–34. (doi:10.1016/j.neuron.2011.06.004)
71. Madisen L *et al.* 2012 A toolbox of Cre-dependent optogenetic transgenic mice for light-induced activation and silencing. *Nat. Neurosci.* **15**, 793–802. (doi:10.1038/nn.3078)
72. Anenberg E, Chan AW, Xie Y, LeDue JM, Murphy TH. 2015 Optogenetic stimulation of GABA neurons can decrease local neuronal activity while increasing cortical blood flow. *J. Cereb. Blood Flow Metab.* **35**, 1579–1586. (doi:10.1038/jcbfm.2015.140)
73. Lee JH, Durand R, Gradinaru V, Zhang F, Goshen I, Kim DS, Fenno LE, Ramakrishnan C, Deisseroth K. 2010 Global and local fMRI signals driven by neurons defined optogenetically by type and wiring. *Nature* **465**, 788–792. (doi:10.1038/nature09108)
74. Kahn I, Desai M, Knoblich U, Bernstein J, Henninger M, Graybiel AM, Boyden ES, Buckner RL, Moore CI. 2011 Characterization of the functional MRI response temporal linearity via optical control of neocortical pyramidal neurons. *J. Neurosci.* **31**, 15 086–15 091. (doi:10.1523/JNEUROSCI.0007-11.2011)
75. Kahn I, Knoblich U, Desai M, Bernstein J, Graybiel AM, Boyden ES, Buckner RL, Moore CI. 2013 Optogenetic drive of neocortical pyramidal neurons generates fMRI signals that are correlated with spiking activity. *Brain Res.* **1511**, 33–45. (doi:10.1016/j.brainres.2013.03.011)
76. Scott NA, Murphy TH. 2012 Hemodynamic responses evoked by neuronal stimulation via channelrhodopsin-2 can be independent of intracortical glutamatergic synaptic transmission. *PLoS ONE* **7**, e29859. (doi:10.1371/journal.pone.0029859)
77. Agulhon C, Petracic J, McMullen AB, Sweger EJ, Minton SK, Taves SR, Casper KB, Fiacco TA, McCarthy KD. 2008 What is the role of astrocyte calcium in neurophysiology? *Neuron* **59**, 932–946. (doi:10.1016/j.neuron.2008.09.004)
78. Koehler RC, Roman RJ, Harder DR. 2009 Astrocytes and the regulation of cerebral blood flow. *Trends Neurosci.* **32**, 160–169. (doi:10.1016/j.tins.2008.11.005)
79. Iadecola C, Nedergaard M. 2007 Glial regulation of the cerebral microvasculature. *Nat. Neurosci.* **10**, 1369–1376. (doi:10.1038/nn2003)
80. Nimmerjahn A. 2009 Astrocytes going live: advances and challenges. *J. Physiol.* **587**, 1639–1647. (doi:10.1113/jphysiol.2008.167171)
81. Petzold GC, Murthy VN. 2011 Role of astrocytes in neurovascular coupling. *Neuron* **71**, 782–797. (doi:10.1016/j.neuron.2011.08.009)
82. Paulson OB, Hasselbalch SG, Rostrup E, Knudsen GM, Pelligrino D. 2010 Cerebral blood flow response to functional activation. *J. Cereb. Blood Flow Metab.* **30**, 2–14. (doi:10.1038/jcbfm.2009.188)
83. Takata N, Nagai T, Ozawa K, Oe Y, Mikoshiba K, Hirase H. 2013 Cerebral blood flow modulation by Basal forebrain or whisker stimulation can occur independently of large cytosolic Ca<sup>2+</sup> signaling in astrocytes. *PLoS ONE* **8**, e66525. (doi:10.1371/journal.pone.0066525)
84. Bonder DE, McCarthy KD. 2014 Astrocytic Gq-GPCR-linked IP3R-dependent Ca<sup>2+</sup> signaling does not mediate neurovascular coupling in mouse visual cortex *in vivo*. *J. Neurosci.* **34**, 13 139–13 150. (doi:10.1523/JNEUROSCI.2591-14.2014)
85. Lind BL, Brazhe AR, Jessen SB, Tan FC, Lauritzen MJ. 2013 Rapid stimulus-evoked astrocyte Ca<sup>2+</sup> elevations and hemodynamic responses in mouse somatosensory cortex *in vivo*. *Proc. Natl Acad. Sci. USA* **110**, E4678–E4687. (doi:10.1073/pnas.1310065110)
86. Otsu Y, Couchman K, Lyons DG, Collot M, Agarwal A, Mallet JM, Pfrieger FW, Bergles DE, Charpak S. 2015 Calcium dynamics in astrocyte processes during neurovascular coupling. *Nat. Neurosci.* **18**, 210–218. (doi:10.1038/nn.3906)
87. Mathiesen C, Brazhe A, Thomsen K, Lauritzen M. 2013 Spontaneous calcium waves in Bergman glia increase with age and hypoxia and may reduce tissue oxygen. *J. Cereb. Blood Flow Metab.* **33**, 161–169. (doi:10.1038/jcbfm.2012.175)
88. Liu X, Li C, Falck JR, Harder DR, Koehler RC. 2012 Relative contribution of cyclooxygenases, epoxyeicosatrienoic acids, and pH to the cerebral blood flow response to vibrissal stimulation. *Am. J. Physiol. Heart Circ. Physiol.* **302**, H1075–H1085. (doi:10.1152/ajpheart.00794.2011)
89. Grubb Jr, RL, Raichle ME, Eichling JO, Ter-Pogossian MM. 1974 The effects of changes in PaCO<sub>2</sub> on cerebral blood volume, blood flow, and vascular mean transit time. *Stroke* **5**, 630–639. (doi:10.1161/01.STR.5.5.630)
90. Magistretti PJ, Pellerin L. 1999 Cellular mechanisms of brain energy metabolism and their relevance to functional brain imaging. *Phil. Trans. R. Soc. Lond. B* **354**, 1155–1163. (doi:10.1098/rstb.1999.0471)
91. Yucel MA, Devor A, Akin A, Boas DA. 2009 The possible role of CO<sub>2</sub> in producing a post-stimulus CBF and BOLD undershoot. *Front. Neuroenerget.* **1**, 7. (doi:10.3389/neuro.14.007.2009)
92. Raichle ME, Mintun MA. 2006 Brain work and brain imaging. *Annu. Rev. Neurosci.* **29**, 449–476. (doi:10.1146/annurev.neuro.29.051605.112819)
93. Dunn KM, Nelson MT. 2010 Potassium channels and neurovascular coupling. *Circul. J.* **74**, 608–616. (doi:10.1253/circj.CJ-10-0174)
94. Filosa JA, Bonev AD, Straub SV, Meredith AL, Wilkerson MK, Aldrich RW, Nelson MT. 2006 Local potassium signaling couples neuronal activity to vasodilation in the brain. *Nat. Neurosci.* **9**, 1397–1403. (doi:10.1038/nn1779)
95. Nelson MT, Quayle JM. 1995 Physiological roles and properties of potassium channels in arterial smooth muscle. *Am. J. Physiol.* **268**, C799–C822.
96. Longden TA, Nelson MT. 2015 Vascular inward rectifier K<sup>+</sup> channels as external K<sup>+</sup> sensors in the control of cerebral blood flow. *Microcirculation* **22**, 183–196. (doi:10.1111/micc.12190)
97. Chen BR, Kozberg MG, Bouchard MB, Shaik MA, Hillman EM. 2014 A critical role for the vascular endothelium in functional neurovascular coupling in the brain. *J. Am. Heart Assoc.* **3**, e000787. (doi:10.1161/JAHA.114.000787)
98. Metea MR, Kofuji P, Newman EA. 2007 Neurovascular coupling is not mediated by potassium siphoning from glial cells. *J. Neurosci.* **27**, 2468–2471. (doi:10.1523/JNEUROSCI.3204-06.2007)
99. Odette LL, Newman EA. 1988 Model of potassium dynamics in the central nervous system. *Glia* **1**, 198–210. (doi:10.1002/glia.440010305)
100. Newman EA, Frambach DA, Odette LL. 1984 Control of extracellular potassium levels by retinal glial cell K<sup>+</sup> siphoning. *Science* **225**, 1174–1175. (doi:10.1126/science.6474173)
101. Gordon GR, Choi HB, Rungta RL, Ellis-Davies GC, MacVicar BA. 2008 Brain metabolism dictates the polarity of astrocyte control over arterioles. *Nature* **456**, 745–749. (doi:10.1038/nature07525)
102. Kılıç K *et al.* *In press.* Tools for high resolution *in vivo* imaging of cellular and molecular mechanisms in cortical spreading depression and spreading depolarization. In *Neurobiological basis of migraine*. New York, NY: Wiley. (<https://www.amazon.com/Neurobiological-Basis-Migraine-Turgay-Dalkara/dp/1118967194>)
103. Ding S, Fellin T, Zhu Y, Lee SY, Auberson YP, Meaney DF, Coulter DA, Carmignoto G, Haydon PG. 2007 Enhanced astrocytic Ca<sup>2+</sup> signals contribute to neuronal excitotoxicity after status epilepticus. *J. Neurosci.* **27**, 10 674–10 684. (doi:10.1523/JNEUROSCI.2001-07.2007)
104. Thompson JK, Peterson MR, Freeman RD. 2003 Single-neuron activity and tissue oxygenation in the cerebral cortex. *Science* **299**, 1070–1072. (doi:10.1126/science.1079220)
105. Viswanathan A, Freeman RD. 2007 Neurometabolic coupling in cerebral cortex reflects synaptic more than spiking activity. *Nat. Neurosci.* **10**, 1308–1312. (doi:10.1038/nn1977)
106. Offenhauser N, Thomsen K, Caesar K, Lauritzen M. 2005 Activity-induced tissue oxygenation changes in rat cerebellar cortex: interplay of postsynaptic activation and blood flow. *J. Physiol.* **565**, 279–294. (doi:10.1113/jphysiol.2005.082776)
107. Erecinska M, Silver IA. 2001 Tissue oxygen tension and brain sensitivity to hypoxia. *Respir. Physiol.*

- 128, 263–276. (doi:10.1016/S0034-5687(01)00306-1)
108. Masamoto K, Takizawa N, Kobayashi H, Oka K, Tanishita K. 2003 Dual responses of tissue partial pressure of oxygen after functional stimulation in rat somatosensory cortex. *Brain Res.* **979**, 104–113. (doi:10.1016/S0006-8993(03)02882-8)
109. Sharan M, Vovenko EP, Vadapalli A, Popel AS, Pittman RN. 2008 Experimental and theoretical studies of oxygen gradients in rat pial microvessels. *J. Cereb. Blood Flow Metab.* **28**, 1597–1604. (doi:10.1038/jcbfm.2008.51)
110. Vazquez AL, Fukuda M, Tasker ML, Masamoto K, Kim SG. 2010 Changes in cerebral arterial, tissue and venous oxygenation with evoked neural stimulation: implications for hemoglobin-based functional neuroimaging. *J. Cereb. Blood Flow Metab.* **30**, 428–439. (doi:10.1038/jcbfm.2009.213)
111. Vovenko E. 1999 Distribution of oxygen tension on the surface of arterioles, capillaries and venules of brain cortex and in tissue in normoxia: an experimental study on rats. *Pflugers Arch.* **437**, 617–623. (doi:10.1007/s004240050825)
112. Ances BM, Wilson DF, Greenberg JH, Detre JA. 2001 Dynamic changes in cerebral blood flow, O<sub>2</sub> tension, and calculated cerebral metabolic rate of O<sub>2</sub> during functional activation using oxygen phosphorescence quenching. *J. Cereb. Blood Flow Metab.* **21**, 511–516. (doi:10.1097/00004647-200105000-00005)
113. Vanzetta I, Grinvald A. 1999 Increased cortical oxidative metabolism due to sensory stimulation: implications for functional brain imaging. *Science* **286**, 1555–1558. (doi:10.1126/science.286.5444.1555)
114. Yaseen MA, Srinivasan VJ, Sakadžić S, Wu W, Ruvinskaya S, Vinogradov SA, Boas DA. 2009 Optical monitoring of oxygen tension in cortical microvessels with confocal microscopy. *Opt. Express* **17**, 22 341–22 350. (doi:10.1364/OE.17.022341)
115. Mangia S, Giove F, Tkac I, Logothetis NK, Henry PG, Olman CA, Maraviglia B, Di Salle F, Ugurbil K. 2009 Metabolic and hemodynamic events after changes in neuronal activity: current hypotheses, theoretical predictions and *in vivo* NMR experimental findings. *J. Cereb. Blood Flow Metab.* **29**, 441–463. (doi:10.1038/jcbfm.2008.134)
116. Aubert A, Costalat R. 2002 A model of the coupling between brain electrical activity, metabolism, and hemodynamics: application to the interpretation of functional neuroimaging. *Neuroimage* **17**, 1162–1181. (doi:10.1006/nimg.2002.1224)
117. Almeida R, Stetter M. 2002 Modeling the link between functional imaging and neuronal activity: synaptic metabolic demand and spike rates. *Neuroimage* **17**, 1065–1079. (doi:10.1006/nimg.2002.1234)
118. Sotero RC, Trujillo-Barreto NJ. 2008 Biophysical model for integrating neuronal activity, EEG, fMRI and metabolism. *Neuroimage* **39**, 290–309. (doi:10.1016/j.neuroimage.2007.08.001)
119. Finikova OS, Lebedev AY, Aprelev A, Troxler T, Gao F, Garnacho C, Muro S, Hochstrasser RM, Vinogradov SA. 2008 Oxygen microscopy by two-photon-excited phosphorescence. *Chemphyschem* **9**, 1673–1679. (doi:10.1002/cphc.200800296)
120. Brinas RP, Troxler T, Hochstrasser RM, Vinogradov SA. 2005 Phosphorescent oxygen sensor with dendritic protection and two-photon absorbing antenna. *J. Am. Chem. Soc.* **127**, 11 851–11 862. (doi:10.1021/ja052947c)
121. Lebedev AY, Troxler T, Vinogradov SA. 2008 Design of metalloporphyrin-based dendritic nanoprobe for two-photon microscopy of oxygen. *J. Porphy. Phthalocyanines* **12**, 1261–1269. (doi:10.1142/S1088424608000649)
122. Sakadžić S *et al.* 2010 Two-photon high-resolution measurement of partial pressure of oxygen in cerebral vasculature and tissue. *Nat. Methods* **7**, 755–759. (doi:10.1038/nmeth.1490)
123. Sakadžić S *et al.* 2014 Large arteriolar component of oxygen delivery implies a safe margin of oxygen supply to cerebral tissue. *Nat. Commun.* **5**, 5734. (doi:10.1038/ncomms6734)
124. Devor A *et al.* 2014 Functional imaging of cerebral oxygenation with intrinsic optical contrast and phosphorescent O<sub>2</sub> sensors. In *Optical imaging of cortical circuit dynamics* (eds B Weber, F Helmchen), pp. 225–253. Berlin, Germany: Springer.
125. Lecoq J, Parpaleix A, Roussakis E, Ducros M, Goulam Houssen Y, Vinogradov SA, Charpak S. 2011 Simultaneous two-photon imaging of oxygen and blood flow in deep cerebral vessels. *Nat. Med.* **17**, 893–898. (doi:10.1038/nm.2394)
126. Parpaleix A, Goulam Houssen Y, Charpak S. 2013 Imaging local neuronal activity by monitoring PO<sub>2</sub> transients in capillaries. *Nat. Med.* **19**, 241–246. (doi:10.1038/nm.3059)
127. Kasischke KA, Lambert EM, Panepento B, Sun A, Gelbard HA, Burgess RW, Foster TH, Nedergaard M. 2010 Two-photon NADH imaging exposes boundaries of oxygen diffusion in cortical vascular supply regions. *J. Cereb. Blood Flow Metab.* **31**, 68–81. (doi:10.1038/jcbfm.2010.158)
128. Lyons DG, Parpaleix A, Roche M, Charpak S. 2016 Mapping oxygen concentration in the awake mouse brain. *eLife* **5**, e12024. (doi:10.7554/eLife.12024)
129. Krogh A. 1919 The supply of oxygen to the tissues and the regulation of the capillary circulation. *J. Physiol.* **52**, 457–474. (doi:10.1113/jphysiol.1919.sp001844)
130. Tsai PS, Kaufhold JP, Blinder P, Friedman B, Drew PJ, Karten HJ, Lyden PD, Kleinfeld D. 2009 Correlations of neuronal and microvascular densities in murine cortex revealed by direct counting and colocalization of nuclei and vessels. *J. Neurosci.* **29**, 14 553–14 570. (doi:10.1523/JNEUROSCI.3287-09.2009)
131. Goldman D. 2008 Theoretical models of microvascular oxygen transport to tissue. *Microcirculation* **15**, 795–811. (doi:10.1080/10739680801938289)
132. Atwell D, Laughlin SB. 2001 An energy budget for signaling in the grey matter of the brain. *J. Cereb. Blood Flow Metab.* **21**, 1133–1145. (doi:10.1097/00004647-200110000-00001)
133. Beard DA, Bassingthwaite JB. 2001 Modeling advection and diffusion of oxygen in complex vascular networks. *Ann. Biomed. Eng.* **29**, 298–310. (doi:10.1114/1.1359450)
134. Dale AM, Sereno MI. 1993 Improved localization of cortical activity by combining EEG and MEG with MRI cortical surface reconstruction: a linear approach. *J. Cogn. Neurosci.* **5**, 162–176. (doi:10.1162/jocn.1993.5.2.162)
135. Hämäläinen M, Hari R, Ilmoniemi R, Knuutila J, Lounasmaa O. 1993 Magnetoencephalography theory, instrumentation, and applications to noninvasive studies of the working human brain. *Rev. Mod. Phys.* **65**, 413–497. (doi:10.1103/RevModPhys.65.413)
136. Markram H, Toledo-Rodriguez M, Wang Y, Gupta A, Silberberg G, Wu C. 2004 Interneurons of the neocortical inhibitory system. *Nat. Rev. Neurosci.* **5**, 793–807. (doi:10.1038/nrn1519)
137. Nunez PL, Srinivasan R. 2006 *Electric fields of the brain: the neurophysics of EEG*. Oxford, UK: Oxford University Press.
138. Liu AK, Dale AM, Belliveau JW. 2002 Monte Carlo simulation studies of EEG and MEG localization accuracy. *Hum. Brain Mapp.* **16**, 47–62. (doi:10.1002/hbm.10024)
139. Einevoll GT, Kayser C, Logothetis NK, Panzeri S. 2013 Modelling and analysis of local field potentials for studying the function of cortical circuits. *Nat. Rev. Neurosci.* **14**, 770–785. (doi:10.1038/nrn3599)
140. Pettersen KH, Devor A, Ulbert I, Dale AM, Einevoll GT. 2006 Current-source density estimation based on inversion of electrostatic forward solution: effects of finite extent of neuronal activity and conductivity discontinuities. *J. Neurosci. Methods* **154**, 116–133. (doi:10.1016/j.jneumeth.2005.12.005)
141. Bangerter NB, Schomer DL, Dehghani N, Ulbert I, Cash S, Papavasiliou S, Eisenberg SR, Dale AM, Halgren E. 2010 Experimental validation of the influence of white matter anisotropy on the intracranial EEG forward solution. *J. Comput. Neurosci.* **29**, 371–387. (doi:10.1007/s10827-009-0205-z)
142. Einevoll GT, Pettersen KH, Devor A, Ulbert I, Halgren E, Dale AM. 2007 Laminar population analysis: estimating firing rates and evoked synaptic activity from multielectrode recordings in rat barrel cortex. *J. Neurophysiol.* **97**, 2174–2190. (doi:10.1152/jn.00845.2006)
143. Jiang X, Wang G, Lee AJ, Stornetta RL, Zhu JJ. 2013 The organization of two new cortical interneuronal circuits. *Nat. Neurosci.* **16**, 210–218. (doi:10.1038/nn.3305)
144. Ascoli GA, Donohue DE, Halavi M. 2007 NeuroMorpho.org: a central resource for neuronal morphologies. *J. Neurosci.* **27**, 9247–9251. (doi:10.1523/JNEUROSCI.2055-07.2007)
145. Kawaguchi Y, Kubota Y. 1996 Physiological and morphological identification of somatostatin- or vasoactive intestinal polypeptide-containing cells among GABAergic cell subtypes in rat frontal cortex. *J. Neurosci.* **16**, 2701–2715.
146. Karagiannis A, Gallopin T, David C, Battaglia D, Geoffroy H, Rossier J, Hillman EM, Staiger JF, Cauli B. 2009 Classification of NPY-expressing neocortical interneurons. *J. Neurosci.* **29**, 3642–3659. (doi:10.1523/JNEUROSCI.0058-09.2009)

147. Ma Y, Hu H, Berrebi AS, Mathers PH, Agmon A. 2006 Distinct subtypes of somatostatin-containing neocortical interneurons revealed in transgenic mice. *J. Neurosci.* **26**, 5069–5082. (doi:10.1523/JNEUROSCI.0661-06.2006)
148. Wang Y, Toledo-Rodriguez M, Gupta A, Wu C, Silberberg G, Luo J, Markram H. 2004 Anatomical, physiological and molecular properties of Martinotti cells in the somatosensory cortex of the juvenile rat. *J. Physiol.* **561**, 65–90. (doi:10.1113/jphysiol.2004.073353)
149. Perrenoud Q, Geoffroy H, Gauthier B, Rancillac A, Alfonsi F, Kassaris N, Rossier J, Vitalis T, Gallopin T. 2012 Characterization of Type I and Type II nNOS-expressing interneurons in the barrel cortex of mouse. *Front. Neural Circuits* **6**, 36. (doi:10.3389/fncir.2012.00036)
150. Linden H, Pettersen KH, Einevoll GT. 2010 Intrinsic dendritic filtering gives low-pass power spectra of local field potentials. *J. Comput. Neurosci.* **29**, 423–444. (doi:10.1007/s10827-010-0245-4)
151. Leski S, Linden H, Tetzlaff T, Pettersen KH, Einevoll GT. 2013 Frequency dependence of signal power and spatial reach of the local field potential. *PLoS Comput. Biol.* **9**, e1003137. (doi:10.1371/journal.pcbi.1003137)
152. Lee AJ *et al.* 2015 Canonical organization of layer 1 neuron-led cortical inhibitory and disinhibitory interneuronal circuits. *Cereb. Cortex* **25**, 2114–2126. (doi:10.1093/cercor/bhu020)
153. Silberberg G, Markram H. 2007 Disynaptic inhibition between neocortical pyramidal cells mediated by Martinotti cells. *Neuron* **53**, 735–746. (doi:10.1016/j.neuron.2007.02.012)
154. Gratiy SL, Devor A, Einevoll GT, Dale AM. 2011 On the estimation of population-specific synaptic currents from laminar multielectrode recordings. *Front. Neuroinform.* **5**, 32. (doi:10.3389/fninf.2011.00032)
155. Hagen E, Dahmen D, Stavrinou ML, Lindén H, Tetzlaff T, van Albada SJ, Grün S, Diesmann M, Einevoll GT. In press. Hybrid scheme for modeling local field potentials from point-neuron networks. *Cereb. Cortex.*
156. Reimann MW, Anastassiou CA, Perin R, Hill SL, Markram H, Koch C. 2013 A biophysically detailed model of neocortical local field potentials predicts the critical role of active membrane currents. *Neuron* **79**, 375–390. (doi:10.1016/j.neuron.2013.05.023)
157. Larkum ME, Kaiser KM, Sakmann B. 1999 Calcium electrogenesis in distal apical dendrites of layer 5 pyramidal cells at a critical frequency of back-propagating action potentials. *Proc. Natl Acad. Sci. USA* **96**, 14 600–14 604. (doi:10.1073/pnas.96.25.14600)
158. Buxton RB, Frank LR, Wong EC, Siewert W, Warach S, Edelman RR. 1998 A general kinetic model for quantitative perfusion imaging with arterial spin labeling. *Magn. Reson. Med.* **40**, 383–396. (doi:10.1002/mrm.1910400308)
159. Liu TT, Brown GG. 2007 Measurement of cerebral perfusion with arterial spin labeling: Part 1. Methods. *J. Int. Neuropsychol. Soc.* **13**, 517–525. (doi:10.1017/S1355617707070646)
160. Wong EC, Buxton RB, Frank LR. 1998 Quantitative imaging of perfusion using a single subtraction (QUIPSS and QUIPSS II). *Magn. Reson. Med.* **39**, 702–708. (doi:10.1002/mrm.1910390506)
161. Liu AK, Belliveau JW, Dale AM. 1998 Spatiotemporal imaging of human brain activity using functional MRI constrained magnetoencephalography data: Monte Carlo simulations. *Proc. Natl Acad. Sci. USA* **95**, 8945–8950. (doi:10.1073/pnas.95.15.8945)
162. Buxton RB, Wong EC, Frank LR. 1998 Dynamics of blood flow and oxygenation changes during brain activation: the balloon model. *Magn. Reson. Med.* **39**, 855–864. (doi:10.1002/mrm.1910390602)
163. Mandeville JB, Marota JJ, Ayata C, Zaharchuk G, Moskowitz MA, Rosen BR, Weisskoff RM. 1999 Evidence of a cerebrovascular postarteriole windkessel with delayed compliance. *J. Cereb. Blood Flow Metab.* **19**, 679–689. (doi:10.1097/00004647-199906000-00012)
164. Gagnon L, Sakadžić S, Lesage F, Pouliot P, Dale AM, Devor A, Buxton RB, Boas DA. 2016 Validation and optimization of hypercapnic-calibrated fMRI from oxygen-sensitive two-photon microscopy. *Phil. Trans. R. Soc. B* **371**, 20150359. (doi:10.1098/rstb.2015.0359)
165. Griffeth VE, Buxton RB. 2011 A theoretical framework for estimating cerebral oxygen metabolism changes using the calibrated-BOLD method: modeling the effects of blood volume distribution, hematocrit, oxygen extraction fraction, and tissue signal properties on the BOLD signal. *Neuroimage* **58**, 198–212. (doi:10.1016/j.neuroimage.2011.05.077)
166. Oberheim NA *et al.* 2009 Uniquely hominid features of adult human astrocytes. *J. Neurosci.* **29**, 3276–3287. (doi:10.1523/JNEUROSCI.4707-08.2009)
167. Nimchinsky EA, Gilissen E, Allman JM, Perl DP, Erwin JM, Hof PR. 1999 A neuronal morphologic type unique to humans and great apes. *Proc. Natl Acad. Sci. USA* **96**, 5268–5273. (doi:10.1073/pnas.96.9.5268)
168. Testa-Silva G, Verhoog MB, Linaro D, de Kock CP, Baayen JC, Meredith RM, De Zeeuw CI, Giugliano M, Mansvelder HD. 2014 High bandwidth synaptic communication and frequency tracking in human neocortex. *PLoS Biol.* **12**, e1002007. (doi:10.1371/journal.pbio.1002007)